2019

Multiscale investigations into reinforced concrete shear wall buildings

Tong Tong
Iowa State University

Multiscale investigations into reinforced concrete shear wall buildings

by

Tong Tong

A thesis submitted to the graduate faculty

in partial fulfillment of the requirements for the degree of

MASTER OF SCIENCE

Major: Civil Engineering (Structural Engineering)

Program of Study Committee:
In-Ho Cho, Major Professor
An Chen
Jarad Niemi

The student author, whose presentation of the scholarship herein was approved by the program of study committee, is solely responsible for the content of this thesis. The Graduate College will ensure this thesis is globally accessible and will not permit alterations after a degree is conferred.

Iowa State University

Ames, Iowa

2019

To Reggie, my husband, my parents, my grandparents, and other family members.

Thank you for enveloping me in love and kindness.

You taught me how to see myself.

TABLE OF CONTENTS

Page

LIST OF FIGURES

Page

ACKNOWLEDGMENTS

I would like to thank my committee chair, Dr. In ho Cho, and my committee members, Dr. An Chen, and Dr. Jarad Niemi, for their guidance and support throughout the course of this research. Their valuable suggestions and great insight in statistical analysis and civil engineering design always inspired me.

I would like to express my heartfelt gratitude to the instructors of the courses I took in Iowa State University, Dr. Jiehua Shen, Dr. Simon Laflamme and Dr. Vivekananda Roy provide, for their well-organized and delightful courses which are always instructive to me.

In addition, I would also like to thank my friends Yicheng Yang and Yinglong Zhang and the department faculty and staff for making my time at Iowa State University a wonderful experience. I want to also offer my appreciation to those who were willing to participate in my surveys and observations, without whom, this thesis would not have been possible.

Last, I want to thank myself for my efforts and persistence. Everything I did about study and research is worthy.

ABSTRACT

Reinforced concrete shear wall (RCSW) is important lateral force-resisting mechanism and widely used in buildings and infrastructure designed before 1980. In the recent extreme earthquake in Chile and Japan, the unexpected dynamic behavior attracted the attention. To finding the relationship between the unexpected dynamic behavior or damage and the height of RCSW building, the novel parallel three-stage multiscale finite element dynamic analysis is used which offers a novel technique that can link millimeter length scale's microphysical damage phenomenon to the building-level non-linear dynamic response with a unidirectional seismic load. There are four different height building as target buildings (4-story building, 8-story building, 12-story building, 16-story building). In the multiscale dynamic analysis, the macroscopic and microscopic damage can be performed at the same time to find the different scales' damage. Results show that the height of the building can affect the tensile and yield condition, inter-story drift ratio, and shear force redistribution.

The thesis is structured as follows. CHAPTER 1 introduces the background of the research, the nonlinear dynamic analysis platform and nonlinear material models used in the research. CHAPTER 2 introduces the pre-processing and post-processing strategy of the parallel three-stage multiscale finite element dynamic analysis. CHAPTER 3 presents the results of the analysis and relative discussion of the results, and the validation of the dynamic analysis model. CHAPTER 4 illustrates limitation and future work.

CHAPTER 1. INTRODUCTION

1.1 Reinforced Concrete Shear Wall

Reinforced concrete shear wall system (RCSW) has served as primary lateral force-resisting mechanism to provide lateral resistance and rotation control in a large portion of buildings and infrastructures normally designed and built before 1980. In the result of survey from *The Concrete Coalition* program that estimates the number of pre-1980 concrete building in twenty-three California counties with the highest seismicity and population, it assesses the risk for the non-ductile concrete building and provides strategies to induce that risk. The number of the public school building where the concrete shear wall used is seven hundred and eighty-six that is fifty-three percentages in the total number of the concrete public school built before 1980. There are three hundred and forty state agency buildings with concrete shear walls from the data compiled by the Department of General Services (DGS, 2008); the seventy-seven court facilities used concrete shear wall structure; there are thirty-six count-eligible buildings in Career Point University (CPU) campus and only one building has not concrete shear walls. Concrete shear wall structure is widely used as lateral-force-resisting system. However, the earthquake loading design and seismic provisions changed in the 1970's [1], the early design of concrete shear wall structure has defective details which may cause the building vulnerable to seismic hazard, which is displayed in the recent earthquake. With the advanced computational tools for design and structural analyses, the design practice of RCSW building has been gradually changed. In Chile, the reinforced concrete shear wall as lateral load resistance mainly utilizes in the building over four floors. Based on the good performance of reinforced concrete building in the March 1985 earthquake, the newer building with the similar the ratio of wall cross-sectional area to floor plan area which is around 3% has thinner wall

and taller buildings with higher wall axial load ratios (up to $0.2A_gf_c$' to $0.4A_gf_c$') [2]. However, recent devastating earthquakes in Japan, Chile, and New Zealand raise significant questions regarding RCSW buildings' unexpected dynamic behaviors. On February 27, 2010, an M_w 8.8 earthquake struck the central south region of Chile. Because the large number of mid- to high-rise buildings in Chile constructed of reinforced concrete with thinner wall followed the modern code, and the most of these buildings rely on reinforced concrete shear wall system to resist lateral or seismic loads. Under the extremely strong shaking, these RCSW buildings appeared unexpected and complicated dynamic damage. The most of the catastrophic damage occurred in the ground story that has some irregular layout. There is also some localized damage happened in the lower floor of the RCSW buildings. These damages lead the buildings collapse suddenly [3]. On March 11, 2011, an M_w 9.0 earthquake occurred off the Sanriku coast of Japan named Tohoku-Oki. The apartment buildings constructed with reinforced concrete in the early 1970s in the disaster area, which damaged at the site where the ground motion amplified right at its characteristic vibration [4]. The duration of earthquake motion was prolonged lead to resulted in the building response has long durations and large amplitudes. The strenuous seismic intensity gave rise to initially stiff RCSW buildings observed dramatically shift to highly flexible state as well as the rarely long duration. The induced flexibility of RCSE buildings resulted in almost a twofold increase in the fundamental period, which corresponded to a significant stiffness reduction [5]. Based on the real building damage in the catastrophic earthquake, degradation of primary core walls and subsequent damage redistributions over the building height and floor-wide structural elements may be collectively associated with complex damage behaviors of RCSW buildings. Hence, there exists a strong

demand for in-depth investigations into the complex damage mechanisms at multiple scales– from a primary core wall level to the floor level, and even to the entire RCSW building level.

The computational investigation used for the dynamic behavior of RCSW building is significantly important for seismic load design and hazard mitigation. Macroscopic models for complex shear wall system are practical and efficient. The common way is using a beam-column element model and consists of an elastic flexural element with a nonlinear rotational spring at each end to account for the inelastic behavior of critical regions [6]. Macroscopic models are the widespread and traditional approach used for a complex shear wall system. For instance, a macroscopic moment-curvature model is used in the investigation of the dual-plastic hinge design concept for reducing higher-mode effects on high-rise cantilever wall buildings, it shows a good performance to compare dual-plastic hinge design approach and single plastic hinge design approach [7]. It is also used for modeling the performance of tall concrete core-wall building under a series of earthquake ground motions representative of very frequent to very rare shaking intensities which is a combination of fiber-section model and nonlinear shear spring. [8]. Even if such macroscopic models provide a valuable understanding of qualitative dynamic behavior of RCSW structure, there are still some challenges remain when the target RCSW building contains complex or irregular geometry. There are lots of kind of complex shear wall and complex asymmetrical structure, such as T-, L- and U-sections or even more complex cross sections of core walls. The behavior of them is complex and relatively unknown as compared to rectangular wall although they are used widely in practice [10]. In 2011, the French Atomic Energy and Sustainable Energies Commission (CEA) and Electricite De France (EDF) began a program entitled “Seismic design and best-estimate Methods Assessment for Reinforced concrete buildings subjected to Torsion and nonlinear

effect" (SMART), which is aim to test asymmetrical structure (1/4-scale 3-story reinforced concrete model) in real seismic scenarios to quantify the effects of nonlinearities and torsion in the dynamic response of the equipment and secondary structure and improve the representativeness of the seismic loading regarding real seismic scenarios. It used AZALEE shaking table and got that only small nonlinearities and both displacement and acceleration – based quantities were properly estimated by model [11]. In an experiment from the University of Tokyo, multi-axial loading is considered to simulate strong motion from an earthquake since the current reinforced concrete building is designed by following the seismic design codes specify the earthquake lateral loadings independently in the way along the principal axis of the structure. The performance of the reinforced concrete wall was tested under uni-axial and bi-axial loading conditions. It reveals weak and complex nonlinear behavior of non-rectangular RCSW system. At the ELSA laboratory, there is a similar experiment. Three same dimensions and reinforced U-shaped walls were loaded in three different directions under lateral cyclic loading. There are multi –cracks happened under different directions loading and bar buckling in compression [12]. According to the above-described experiments, the complexity of geometry, loading direction, and multifaceted nonlinear degradation phenomena are all needed to consider and incorporate into the building's dynamic motions when the unexpected weak dynamic behavior of RCSW buildings occurs under extreme earthquakes.

In what follows, the adopting multiscale analysis approach in this research will explain. The central notions of three-tiered multiscale dynamic analysis platform and advanced parallel computing algorithms shall be touched upon, all of which are essential to realize the novel multiscale dynamic analysis. Computational investigation results will be present over multiple length scales, spanning building, floor, and individual complex walls.

1.2 Multiscale Analysis

For right now, the principal goal is to better understand the source and development of "unexpected" dynamic response of RCSW buildings by making use of novel "multiscale" dynamic analyses to cover the shortage of macroscopic analyses [13]. The term "multiscale" came from mathematics and physics, which is a technique used to construct uniformly valid approximations to the solutions of perturbation problems. In this research, it means the novel nonlinear dynamic analysis of RCSW building that analysis the millimeter length scale's and large length scale's physical damage directly affect the building-level dynamic response. Previously, multiscale modeling application to an individual wall element has been carried out in Italy. There is much uncertainty about both the seismic demand and the seismic capacity of the structure which makes difference to assess the performance of the building designed for an earthquake with different intensities. Thus, the multiple performance objectives need be considered to cope with the levels of seismic hazard, which could include displacements, forces, ductility, strains, etc. A multi-level design procedure that can predict not only the structural behavior at collapse but also the non-linear response due to more frequent and less damaging earthquakes arise in need. It adopts different scales of the structure modeling inside the framework of the pushover analysis, connecting the studies on analysis procedures with those on modeling strategies. In an early experiment listed in Reynouard's book, the two parallel 5-stories RC walls without opening, connected by six square floors. In the micro-scale approaches, the most accurate modeling approach of the finite element method named EF2002 combined with an incremental Newton-type solution strategy was adopted to perform the non-linear analysis of RC structural element in the plane state of stress under quasi-static loading that means time and inertial force are irrelevant. In the meso-scale approaches, a displacement-

based beam-column fiber element named RCIZ has been adopted to represent the cyclic shear behavior and resistance of RC structural element under seismic excitation [6]. However, the clear novelty of the present multiscale analysis lies in the extended link from millimeter-length scale to the entire RCSW building scale. Through this novel link, a dynamic motion of RCSW building can be investigated and explained through some various microscopic phenomena, such as including nonlinear shear resulting from aggregate-cement interlocking on multidirectional cracks, progressive bar buckling accompanied by spalling and crushing, and so on [13]. In the following, the basic information of multiscale analysis will be introduced.

1.2.1 Macro- and meso- level analysis

The macro-level analysis does for the global dynamic response of MDOF system. The motion of the macro-level system is constructed by the equation below including a damping matrix **C:**

$$\boldsymbol{M\ddot{u} + C\dot{u} + ku = -M1\ddot{u}_g(t)} \tag{1}$$

where

$$\boldsymbol{M}_{[3N\times 3N]} = \begin{bmatrix} \boldsymbol{m}_1 & & \\ & \ddots & \\ & & \boldsymbol{m}_N \end{bmatrix}, \quad \boldsymbol{m}_j = \begin{bmatrix} m_j & & \\ & m_j & \\ & & I_{Oj} \end{bmatrix}, \quad \mathbf{1}_{[3N\times 2]} = \begin{bmatrix} 1 & 0 \\ 0 & 0 \\ 0 & 1 \\ \vdots & \vdots \\ 1 & 0 \\ 0 & 0 \\ 0 & 1 \end{bmatrix}, \tag{2}$$

$$\ddot{\boldsymbol{u}}_{\boldsymbol{g}} = \begin{Bmatrix} \ddot{\boldsymbol{u}}_{gx}(t) \\ \ddot{\boldsymbol{u}}_{gy}(t) \end{Bmatrix}$$

I_{Oj} is the moment of inertia of the j th diaphragm, $\boldsymbol{k}$ is the stiffness matrix, $\ddot{\boldsymbol{u}}_{\boldsymbol{g}}$ is the ground acceleration.

For meso-level analysis, the target needs to be analyzed is each floor. In a floor of the building, there are lots of structural components used to resisting lateral loadings. For i th floor, the new incremental internal forces would be defined by integrating resisting forces of all structural components on the floor:

$$\Delta \boldsymbol{F}_i = \int \Delta \boldsymbol{F}_j^{mc} \tag{3}$$

where $\Delta \boldsymbol{F}_j^{mc}$ stands for the incremental internal force vector of the j th structural component on the domain A_j^{mc} which belongs to A_i which is the domain of $\Delta \boldsymbol{F}_i$. Since the nonlinearity is related with the complicated deterioration mechanisms such as localized crushing, progressive bar buckling, and multiple cracks, the micro-level analysis is necessary.

To find the incremental internal force vector of the j th structural component, the equilibrium was built with the constraint condition which is the incremental displacement at the boundary of the micro-level system ($\Delta \boldsymbol{u}_j^{mc}$ at the boundary of j th structural component). To satisfy the new equilibrium and Equation (4), the penalty method was adopted in the context of the constrained variational problem [14]. Each structural component domain A_j^{mc} constitutes one partition within a sub-domain A_i.

$$\text{the micro} - \text{level boundary problem} \begin{bmatrix} \boldsymbol{K}_j^{mc} \Delta \boldsymbol{d}(t) = \Delta \boldsymbol{F}_j^{mc} \ \text{equilibrium on} \ A_j^{mc} \\ \Delta \boldsymbol{u}_j^{mc} = \boldsymbol{a}_j^{mc} \Delta \boldsymbol{d}_{\boldsymbol{i}}(t) \ \text{constraint at} \ \Gamma_j^{mc} \end{bmatrix} \tag{4}$$

where $\boldsymbol{K}_j^{mc}$ is the tangent stiffness of the micro-level system, $\Delta \boldsymbol{d}(t)$ is the incremental displacement, $\boldsymbol{a}_j^{mc}$ is a transformation matrix relating meso-level to micro-level. The micro-

level domain is denoted by A_j^{mc} of which is restrained by Γ_j^{mc} . $\Delta \boldsymbol{F}_j^{mc}$ is the incremental resisting force at Γ_j^{mc} , which is generally given by:

$$\Delta \boldsymbol{F}_j^{mc} = \int \rho_0 \boldsymbol{N} \boldsymbol{b} dA_j^{mc} + \int \boldsymbol{N}\, \Delta \boldsymbol{t} d\Gamma_j^{mc} \tag{5}$$

where ρ_0 is the initial density, $\boldsymbol{b}$ is the body force per unit mass, $\boldsymbol{N}$ is the shape function, and $\Delta \boldsymbol{t}$ is the external boundary traction. To concurrently satisfy the two conditions of Equation (4), the stationary condition of a new function need to found

$$Y(\boldsymbol{d}) = \left(\frac{\Delta \boldsymbol{d}^T (\boldsymbol{K}_j^{mc})^T \Delta \boldsymbol{d}}{2} - \Delta \boldsymbol{d}^T \Delta \boldsymbol{F}_j^{mc} \right) + \left(\frac{\lambda_p}{2} \left(\mathbf{1}_p^T \Delta \boldsymbol{d} - \mathbf{1}_p^T \Delta \boldsymbol{u}_j^{mc} \right)^2 \right) \tag{6}$$

where λ_p is a large stiffness of the penalty element. Through modifying the equation, the following equation is obtained:

$$\left\{ \boldsymbol{K}_j^{mc} + \lambda_p \mathbf{1}_p \mathbf{1}_p^T \right\} \Delta \boldsymbol{d}(t) = \Delta \boldsymbol{F}_j^{mc} + \lambda_p \mathbf{1}_p^T \Delta \boldsymbol{u}_j^{mc}(t) \mathbf{1}_p \tag{7}$$

where $\mathbf{1}_p$ has una it entity to the DOF of nodes on which displacement constraint is imposed.

Physically, the penalty elements represent virtual elastic springs whose stiffness is defined by $\lambda_p \gg \max(\boldsymbol{K}_j^{mc})$.

1.2.2 Micro-level analysis

In the micro-level analysis, the concrete and space truss of each structural component would be meshed by finite hexagonal solid elements which contains random-sized rigid particles at its integration points and soft matrix. At each integration point, the local constitutive response is defined by physical mechanisms on the framework of the

multidirectional smeared crack model. Meanwhile, the current strain is passed to microphysical mechanism-based models such as multi-directional crack model, nonlinear interlocking model, nonlocal information-based confinement model, and so on, to update new stresses. There are at most three the orthogonal cracks can develop. The microscopic stress tensor $\boldsymbol{\sigma}^{cr} \coloneqq \langle \sigma_1^{cr} \quad \sigma_2^{cr} \quad \sigma_3^{cr} \quad \sigma_{12}^{cr} \quad \sigma_{23}^{cr} \quad \sigma_{13}^{cr} \ \ldots\ldots \rangle^T$ is determined by a micro-stress functions $\sigma_i^{cr} \coloneqq \Psi(e_i^{cr})$, the crack normal stress s_i^{cr} on the i th crack surface is also derived from the micro-stress functions. The Ψ represents the Thorenfeldt compression model and Moelands and Reinhardt model for the nonlinear tensile regime [15]. Between rigid particle and soft matrix, the interlocking mechanism is used for the shear stress on a crack surface

$$\tau_{ij}^{cr} \coloneqq G(\tilde{\varepsilon})\gamma_{ij}^{cr} \tag{8}$$

where the tangent shear stiffness is mathematically derived from the active contact area of particle and soft-matrix:

$$G(\tilde{\varepsilon}) = C_{CS}\frac{G_0}{(1+\mu)}\frac{2}{\pi}\left\{\arctan\sqrt{\tilde{\varepsilon}^{-2}-1} - \tilde{\varepsilon}\sqrt{1-\tilde{\varepsilon}^2} + \frac{2}{\pi}\mu(1-\tilde{\varepsilon}^2)\right\} \tag{9}$$

$$\tilde{\varepsilon} = 2d/D_{\max} \times \max(\varepsilon_i^{cr}, \varepsilon_j^{cr}) \tag{10}$$

where G_0 is the elastic shear modulus, μ is fra iction coefficient which is 0.4, C_{CS} is experimental calibration which equals 1.66×10^{-4}, d is current crack gap distance, $D_{\max}$ is the diameter of the rigid particle randomly generated from the Normal distribution, $N(0.019,0.00633^2)$.

To update the new internal force after one-time strep, the current stress is integrated:

$$\mathbf{F}_{\text{internal}}^{i} = \sum_{k=1}^{p-1} \mathbf{F}_{\text{internal},k}^{i} = \sum_{k=1}^{p-1} \left(\int \mathbf{B}^{\mathrm{T}} \boldsymbol{\sigma}_{c}^{i} dV_k + \int \mathbf{B}^{\mathrm{T}} \boldsymbol{\sigma}_{s}^{i} dV_k \right) \tag{11}$$

where i is local time step, $\boldsymbol{F}_{internal}^{i}$ is the internal force vector defined on the sub-master in the parallel computing; $\boldsymbol{F}_{internal,k}^{i}$ is the internal force vector defined on the processor P_k; p is the number of total processors of the present sub-group, the integration parts are in the domain V_k that is a partition of structure assigned to P_k. $\boldsymbol{B}$ is strain-displacement matria x, $\boldsymbol{\sigma}_{c}^{i}$ and $\boldsymbol{\sigma}_{s}^{i}$ separately stand for current concrete and steel stresses evaluated.

1.3 The Program of Microscopic analysis: Virtual Earthquake Engineering Tool (VEEL)

For filling the gap between simulation capacity and actual damage and failure modes of real structure during big earthquakes and settling the unresolved question that is nonlinear shear, localized damage and progressive buckling of reinforcing bars, a novel parallel simulation platform named Virtual Earthquake Engineering Laboratory (VEEL) is developed by Dr. Cho using C++ program that is a common software development language and Message Passing Interface (MPI) that is a library specification for message-passing to create parallel computing architecture, which is the inclusion of the microscopic parallel multiscale FEA engine. In the multilinear wall models of macroscopic analysis, VEEL can be used as nonlinear hysteretic models for box-shaped walls, L-shaped walls, rectangular walls, and RC columns on each floor. [15] Meanwhile, the VEEL can capture multi-directional micro-cracks, progressive bar buckling, general confinement effect, non-linear shear of cracked concrete

based on the interlocking of random-sized particles etc. VEEL was used in this study to do the microscopic analysis.

1.4 Nonlinear Material Models

1.4.1 "Smart" Steel Model

"Smart" reinforcing steel model is designed with general applicability, which is mostly used to deal with microstates of surrounding materials, topological change of the reinforced system, etc. It provides a clear evolution of the bar buckling length of longitudinal steel bars.

The base unit BU_i is defined to systematically study the evolution of buckling length of longitudinal steel bar, which is consists of the i_{th} steel bar and a set of its surrounding elements S_i ($i \in [1, n_i]$, n_i is the total number of steel bars). The change of buckling length is linked with the topological transition that can be triggered only when all surrounding elements enter at least partially crushed state. After losing surrounding elements, the bars can coalesce with adjacent bars to construct new base unit pivoting around the lengthened bar. Topological transition of BU_m is related to the dissipated energy of surrounding elements in S_m:

$$\int_{S_m} \sigma dV \geq E_{th} \tag{12}$$

where E_{th} is a specific energy threshold. Meanwhile, two internal state variables are introduced to define the energy state of the material. One is at the integration point level, the variable $a_i^{(k)}$ is described:

$$a_i^{(k)} = \begin{cases} 1 & for \ \min_t \varepsilon_k^{cr} > \varepsilon_{th} \\ 2 & otherwise \end{cases} \tag{13}$$

where ε_{th} is strain threshold for entering crushing phase. The other internal state is defined as element level whose variable λ_j is also defined to signify intact, partially crushed, and fully crushed states by using value 0, 1, and 2:

$$\lambda_j = \begin{cases} 0 & \beta_j \leq NINT^{(j)} \times 3 \\ 1 & NINT^{(j)} \times 3 < \beta_j \leq NINT^{(j)} \times 6 \\ 2 & \beta_j \geq NINT^{(j)} \times 6 \end{cases} \quad (14)$$

where $NINT^{(j)}$ = number of integration points of the j_{th} element $\in S_m$. If the elements around the bar are artially crushed, the topological transition is ascertained by:

$$\sum_{j=1}^{n(S_m)} \lambda_j \geq n(S_m) \quad (15)$$

where $n(S_m)$ means the number of entities in S_m. The new buckling length can be found once the above condition is violated, the topological transition is triggered and the buckling length of the corresponding reinforcing bar can evolve by merging with adjacent bars' buckling length:

$$L_b \equiv \sum_{L_0^{(i)} for \forall e_i^1 \in BU_m} k L_0^{(i)} \quad (16)$$

where $L_0^{(i)}$ is initial buckling length of the i_{th}steel bar e_i^1, k is effective length factor (0.5 for fixed boundary condition). Meanwhile, this new buckling length provides the latest information to the process of new buckling initiation point ε^*:

$$\frac{\varepsilon^*}{\varepsilon_y} = 55 - 2.3\sqrt{\frac{f_y}{100}}\frac{L_b}{D_s};\ \frac{\varepsilon^*}{\varepsilon_y} \geq 7 \quad (16)$$

where ε^* is the intermediate strain where buckling initiates, ε_y and f_y are the strain and stress at yielding; L_b is the buckling length updated and D_s is the diameter of the bar cross section. The model is schematically illustrated in Figure 1[15].

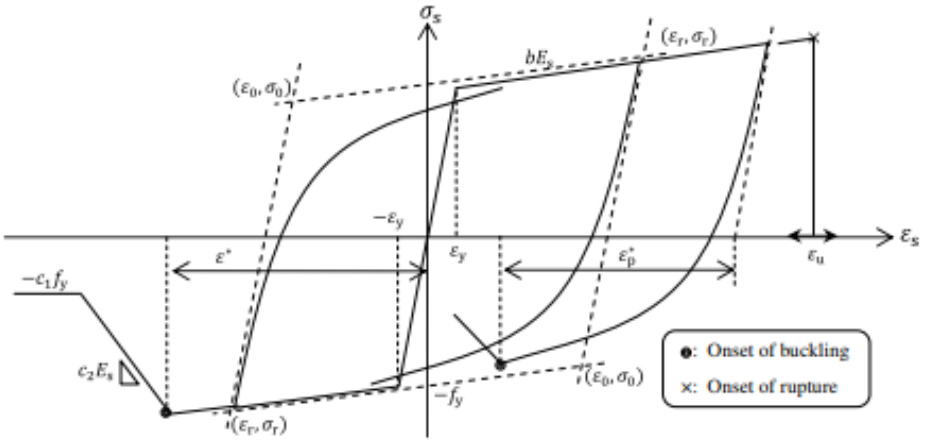

Figure 1. *Stress-strain relationship of the Generalized Menegotto-Pinto bar model (Cited from [15])*

1.4.2 Information-based Concrete Model

The concrete model used in this study is the Modified Thorenfeldt Concrete model with Nonlocal-information-based Confinement Model. The fixed-type multidirectional smeared crack model was introduced in the concrete model, which can describe the nonlinear behavior of the cracked quasi-brittle material. At each loading step, the current total strain can be defined as:

$$\boldsymbol{\varepsilon}^{cr} = \boldsymbol{PT\varepsilon} \tag{17}$$

where $\boldsymbol{T}$ is a ransformation matrix form Eigen analysis of $\boldsymbol{\varepsilon}$. $\boldsymbol{P}$ is matthe rix for the Poisson effect following the equivalent strain method by Feenstra [17]. When the maximum principal

strain is larger than the given strain threshold ε_{th}, a Mode I crack onsets which can be considered

$$max\{eig[\varepsilon(\tau)]\} > \varepsilon_{th} \rightarrow T(t) = T(\tau) \quad for\ \forall t \geq \tau \tag{18}$$

On this basis, the Thorenfeldt concrete model [16] is adopted as a base model for compressive behavior on the crack surfaces. This model supposes be analyzed to be one of the most balanced models with sufficient accuracy and efficiency for the concrete, covering a wide range of strengths. The expression of the model is given below:

$$\sigma_i^{cr} = -f_c' \cdot x\left(\frac{n}{n - 1 + x^{n \cdot k}}\right) \tag{19}$$

where σ_i^{cr} is current normal stress on *i* th crack surface (MPa), $i \in \{1,2,3\}$; f_c' is compressive strength (MPa); x is the ratio of normal strain on *i* th crack surface and strain at the compressive strength,

$$x = \frac{\varepsilon_i^{cr}}{\varepsilon_0} \tag{20}$$

where ε_i^{cr} is normal strain on *i* th crack surface, ε_0 is strain at the compressive strength; n equals 0.80 + f_c'/17; *k* equals 1.0 when $0 > \varepsilon_i^{cr} > \varepsilon_0$ or k equals 0.67 + f_c' / 62 for $\varepsilon_i^{cr} \leq \varepsilon_0$.

Figure 2 is shown the Modified Thorenfeldt Concrete model with Nonlocal-information-based Confinement Model.

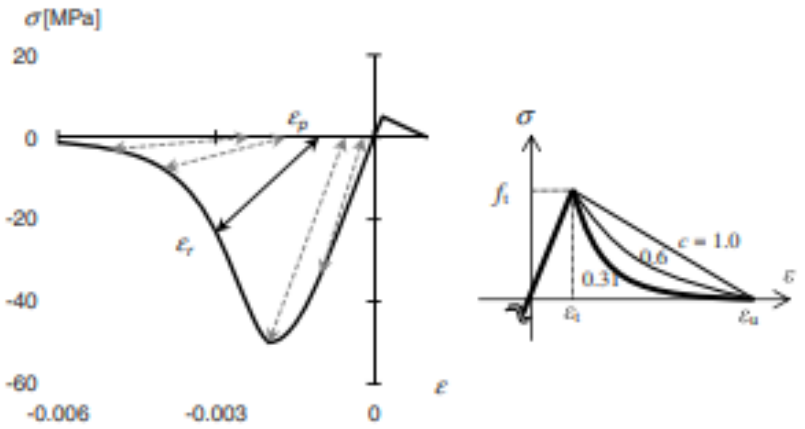

Figure 2. *Modified Thorenfeldt Concrete model with Nonlocal-information-based Confinement Model* (Cited from [15])

1.4.2.1 Information-Based Confinement model

The nonlocal information-based confinement model is also introduced in this concrete model, which is successful to capture the confinement effect in a variety of reinforced concrete structure [29], such as a rectangular or irregular-shape wall with or without opening. By using a modification factor to adjust ε_0 and f_c' as shown in Eq (21), two kinds of strength conditions would be considered. One is the laterally confined structure has an enhanced ε_0 causes quasi-brittle material tends to be resilient, another one is the structure without lateral confinements with pre-damages in a form of lateral micro-cracks which causes the resilience to compression tends to deteriorate:

$$\varepsilon_0 = \alpha\varepsilon_0; \quad f_c' = \beta f_c' \tag{21}$$

There are two exploratory models are suggested in Eq (22). One is step-wise model that is shown as follow:

$$\alpha = \begin{matrix} 1.0 \\ 2.0 \end{matrix}; \quad \beta = \begin{matrix} 1.0 & for & d_{ic} \leq 0.3 \\ 1.0 & for & d_{ic} > 0.3 \end{matrix} \tag{22}$$

The other is an exponential model:

$$\alpha = \begin{matrix} 1.0 \\ exp[3.3(d_{ic} - 0.3)] \end{matrix}; \quad \beta = \begin{matrix} 1.0 & for & d_{ic} \leq 0.3 \\ exp(d_{ic} - 0.3) & for & d_{ic} > 0.3 \end{matrix} \tag{23}$$

where d_{ic} is information index that represent the lateral confinement condition with a single scalar value from 0 to 1 to map any confined conditions.

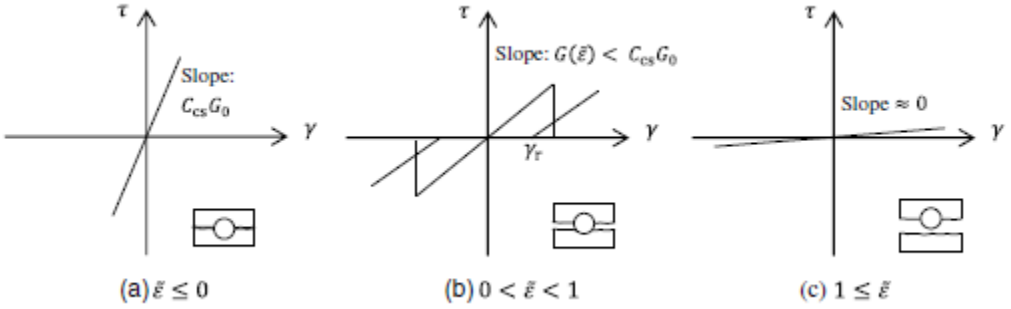

Figure 3. *Variation of tangent shear stiffness depending on crack opening (Cited from [18])*

1.4.2.2 Nonlinear Shear Stiffness

This concrete model can utilize the interlocking mechanism [30] to evaluate nonlinear shear stiffness. When the earthquake occurs, the interaction between moving surfaces may happen the situation in Figure 3, which is the permanent plastic deformation occurs at the soft matrix part only, and the ideal sphere remains intact during the whole cyclic loading process [18]. This movement is tied to the micro-cracking. Assume there is the diameter of an ideal particle D_{max} which causes shear resistance. According to the parameters in Figure 4, since the tangent shear stiffness G has affected by contacting areas A_v and μA_h

$$A_v = \pi c^2/2,\ A_h = (\frac{D_{max}}{2})^2\, arctan\left(\frac{c}{d}\right) - c \times d \tag{24}$$

where $c = \sqrt{(\frac{D_{max}}{2})^2 - d^2}$, d is the distance between crack surfaces. By introducing $\tilde{\varepsilon} = 2d/D_{max}$ and normalizing with $(\frac{D_{max}}{2})^{-2}$, the tangent shear stiffness on crack surface is proposed as

$$G(\tilde{\varepsilon}) = C_{cs}\frac{G_0}{(1+\mu)}\frac{2}{\pi}\left\{arctan\sqrt{\tilde{\varepsilon}^{-2}-1} - \tilde{\varepsilon}\sqrt{1-\tilde{\varepsilon}^2} + \frac{\pi}{2}\mu(1-\tilde{\varepsilon}^2)\right\} \tag{25}$$

where $G_0$is elastic shear modulus, μ is friction coefficient, C_{cs} is reduction factor which is to adjust the strength difference between the rigid particle and the soft matrix, $\tilde{\varepsilon}$ has relatia onship with normal strain to the crack surface ε, that is $\varepsilon = \tilde{\varepsilon}\frac{D_{max}/2}{L}$, L is the length of element.

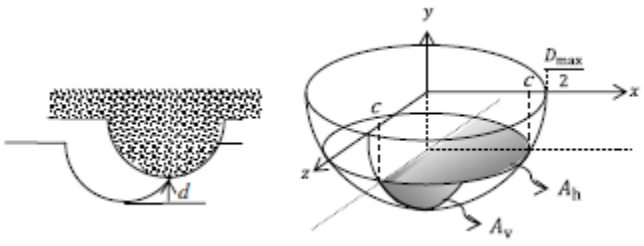

Figure 4. *Projections of the contact area of the ideal hemisphere with a diameter D_{max} (Cited from [18]).*

When the value of $\tilde{\varepsilon}$ is smaller than 0, the maximum tangent shear stiffness can be gain when the crack is closed. When $\tilde{\varepsilon}$ is between 0 to 1, the shear resistance between crack surface is governed by the interlocking mechanism, the tangent shear stiffness develops from shear strain γ_r if the reloading processes, the early resistance gradually disappears as the horizontal displacement increases and the expression of γ_r is

$$\gamma_r = |\gamma_{max}| \times \{a + b(1 - exp(-c \times |\gamma_{max}|))\} \quad for \quad \gamma > 0 \tag{26}$$

where a, b, and c are positive constant with $a + b = 1$ and γ_{max} which is not a fixed number and constantly updated value as time proceeds during nonlinear analysis is the maximum shear strain ever experienced on the crack surface. When $\tilde{\varepsilon}$ is larger than 1, there is no resistance of shear if the crack fully opens more than the half of the ideal particle size.

1.5 Three-Stage Multiscale Nonlinear Dynamic Analysis Platform

The Three-Stage Multiscale Nonlinear Dynamic Analysis Platform is developed by Dr.Cho [10], which can do the nonlinear dynamic analyses for reinforced concrete building containing complex walls under seismic performance at three stage: (1) Micro level, the microscopic nonlinearities can be captured by a microphysical mechanism-based parallel finite element analysis (FEA) engine which is the Virtual Earthquake Engineering Laboratory (VEEL); (2) Meso level, the analysis can show the floor-specific variability and the direct update of simple structural elements assigned with elastic or multilinear models; (3) Macro level, the nonlinear dynamic analysis of the entire building can be done with a reduced degree-of-freedom (DOF) system. The significant feature of the multiscale analysis is the direction of information exchange between scales. The coupled multiscale analysis is the information flows both ways between scales, which allows inter-scale mutual interaction and coherently evolving physical mechanisms; the uncoupled multiscale analysis omits the interaction to make the computation efficient. In the coupled multiscale analysis, the micro level damage can affect the global deformation and vice versa. VEEL can run simultaneously to update incremental resisting forces of individual structural elements by using the coupled one; the micro level is

used only for making an equivalent multilinear model by using the uncoupled one. Figure 5 shows three-stage nonlinear analysis from the microscopic level to macroscopic level.

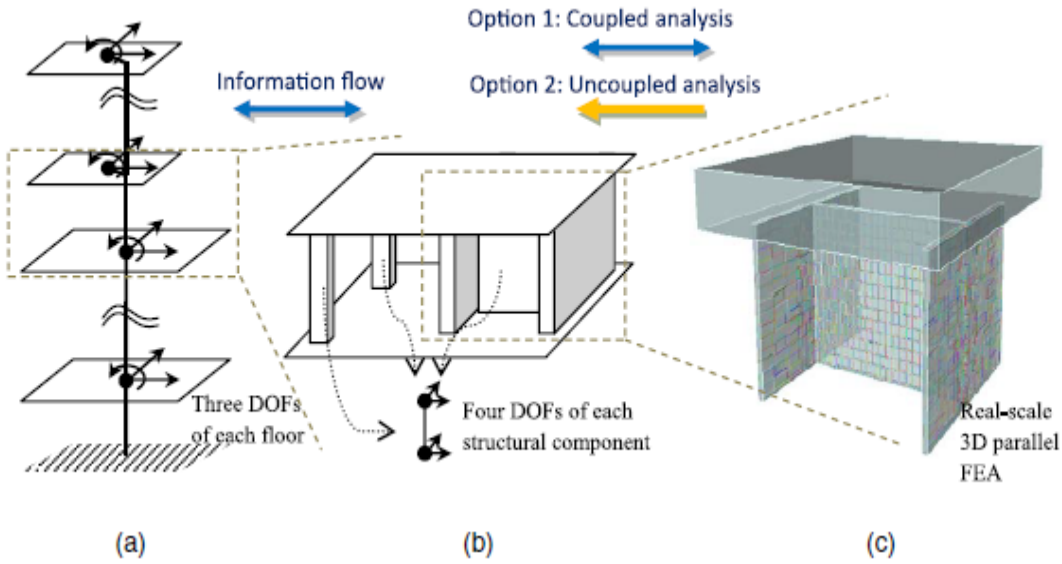

Figure 5. *Three-stage multiscale platform for building-level nonlinear dynamic analyses: (a) macro-level platform for dynamic analyses of a building; (b) meso-level; (c) micro-level platform harnessing VEEL. (Cited from [10])*

1.5.1 Information Transfer between Macro and Meso Level

The floor displacements can be described by two horizontal translations and one torsional rotation. The global displacement vector of a macro-level multiple degrees of freedom (MDOF) system for an N-floor building is

$$\boldsymbol{u}_{[3N\times 1]} = [u_{x1}\ u_{y1}\ u_{\theta 1}\ \cdots\ u_{xj}\ u_{yj}\ u_{\theta j}\ \cdots\ u_{xN}\ u_{yN}\ u_{\theta N}\ ]^T \qquad (27)$$

$$= [\boldsymbol{u_1}\ \cdots\ \boldsymbol{u_j}\ \cdots\ \boldsymbol{u_N}\ ]^T$$

where j means the j th floor of the building. Based on Chopra's direct-stiffness method [20], the structural component of the meso level is assumed to have two horizontal displacements, the local torsional deformation is neglected. The local displacement of column C at meso level

composed by the global displacements of the j th and (j + 1) th floors, and a transformation matrix relates the between global floor displacement at the macro level and the local displacement of each structural component at the meso level represented as $\boldsymbol{a}$:

$$\boldsymbol{u}_{C(J+1)} = \begin{Bmatrix} u_{Cx(J+1)} \\ u_{Cy(J+1)} \end{Bmatrix} = \begin{bmatrix} -1 & 0 & e_{Cyj} & 1 & 0 & -e_{Cy(j+1)} \\ 0 & -1 & e_{Cxj} & 0 & 1 & -e_{Cx(j+1)} \end{bmatrix} \begin{Bmatrix} u_{xj} \\ u_{yj} \\ u_{\theta j} \\ u_{x(j+1)} \\ u_{y(j+1)} \\ u_{\theta(j+1)} \end{Bmatrix} \tag{28}$$

$$= \boldsymbol{a}_{C(J+1)} \begin{Bmatrix} \boldsymbol{u}_j \\ \boldsymbol{u}_{(j+1)} \end{Bmatrix}$$

where (J + 1), $J \in [1, N]$ denotes the local quantities of a structural component residing between the j th and (j + 1) th floors, and e is the eccentricity. Then, the local element stiffness is constructed by

$$\boldsymbol{k}_{C(J+1)} = \boldsymbol{a}^T_{C(J+1)} \boldsymbol{k}_{C(J+1),Local} \boldsymbol{a}_{C(J+1)} \text{ with } \boldsymbol{k}_{C(J+1),Local} = \begin{bmatrix} \boldsymbol{k}_{Cx(J+1)} & 0 \\ 0 & \boldsymbol{k}_{Cy(J+1)} \end{bmatrix} \tag{29}$$

The global stiffness matrix $\boldsymbol{k}_{[3N\times 3N]}$ that is tied to the global displacement $\boldsymbol{u}_{[3N\times 1]}$ can now be constructed by a typical assembly procedure.

According to the translational deformation $u_{Cx(J+1)}$ and $u_{Cy(J+1)}$ in Equation (28), the internal force $F^{int}_{Cx(J+1)}$ and $F^{int}_{Cy(J+1)}$ at meso level can transformed to the corresponding global resisting forces vector of the j th floor at the macro level $\mathbf{F}^{int}_{j[3N\times 1]}$ which is reduced DOF:

$$\begin{Bmatrix} \mathbf{F}^{int}_{j} \\ \mathbf{F}^{int}_{j+1} \end{Bmatrix}_{[6N\times 1]} = \boldsymbol{a}^T_{C(J+1)} \begin{Bmatrix} F^{int}_{Cx(J+1)} \\ F^{int}_{Cy(J+1)} \end{Bmatrix} \tag{30}$$

The updating for information, such as the internal force, can be realized in two options. One (coupled multiscale analysis) is the current displacement information in meso level is

merely passed to the micro level, the meso level receives the newly calculated information from the micro level after solving the three-dimensional (3-D) boundary-value problem with the meso level displacement as a new constraint in micro-level analysis. The second option (uncoupled multiscale analysis) is meso-level directly updates the information with a simple elastic or multilinear hysteresis model which is an equivalent model and perform sufficiently accurate since the parameter values are established to mimic the specific geometry and material properties of the element under consideration.

The motion of the macro-level system is constructed by the equation below including a damping matrix ***C*:**

$$\boldsymbol{M\ddot{u} + C\dot{u} + ku} = -\boldsymbol{M1}\ddot{u}_g(t) \tag{31}$$

where

$$\boldsymbol{M}_{[3N\times 3N]} = \begin{bmatrix} \boldsymbol{m}_1 & & \\ & \ddots & \\ & & \boldsymbol{m}_N \end{bmatrix}, \quad \boldsymbol{m}_j = \begin{bmatrix} m_j & & \\ & m_j & \\ & & I_{Oj} \end{bmatrix}, \quad \mathbf{1}_{[3N\times 2]} = \begin{bmatrix} 1 & 0 \\ 0 & 0 \\ 0 & 1 \\ \vdots & \vdots \\ 1 & 0 \\ 0 & 0 \\ 0 & 1 \end{bmatrix}, \tag{32}$$

$$\ddot{\boldsymbol{u}}_{\boldsymbol{g}} = \begin{Bmatrix} \ddot{u}_{gx}(t) \\ \ddot{u}_{gy}(t) \end{Bmatrix}$$

I_{Oj} is the moment of inertia of the j th diaphragm.

1.5.2 Information Transfer Between Meso and Micro Level

The analysis at the micro level can be regarded as one-step displacement-controlled nonlinear FEA that solves a 3-D boundary-value problem given the displacement constraint. Finding the required incremental force ΔF at the boundaries (such as intersection between a

structural component and floors) that satisfies the incremental displacement Δd at the boundaries and updating new microscopic states, including cracks, progressive bar buckling and so on, are the major objective of the analysis at the micro level. The information transfers from meso to micro level by the incremental displacement at time step *t*. The incremental displacement of the real-scale structure at micro-level can be calculated by:

$$\begin{Bmatrix}\Delta d_{Cx(J+1)}\\ \Delta d_{Cy(J+1)}\end{Bmatrix} = \begin{Bmatrix}u_{Cx(J+1)}\\ \mathrm{u}_{Cy(J+1)}\end{Bmatrix} - \begin{Bmatrix}u_{CxJ}\\ \mathrm{u}_{CyJ}\end{Bmatrix} \tag{33}$$

where $(J+1)$, $J \in [1, N]$ stands for a structural component at the meso-level which locates between the *j* th and (*j* + 1) th floors. $\Delta d_{Cx(J+1)}$ represents the incremental displacement in the x-direction at the micro level which can satisfy the displacement compatibility between micro and meso level for real-scale structure. The nodal displacement vector $\boldsymbol{\Delta d}$ at meso level can be driven the relation, which is shown below:

$$\boldsymbol{\Delta d}_{[n_{ep}\times 1]} = [\mathbf{1}_x \quad \mathbf{1}_y]_{[n_{ep}\times 2]} \begin{Bmatrix}\Delta d_{Cx(J+1)}(t)\\ \Delta d_{Cy(J+1)}(t)\end{Bmatrix}_{[2\times 1]} \tag{34}$$

where $\mathbf{1}_x$ contains unit entities to the DOFs of nodes on which incremental nodal forces are imposed, which can be represented by $\langle 0 \ldots 100 \ldots 100 \ldots 0\rangle^T$. n_{ep} stands for the number of total DOF s of the micro-level system. In a similar way, the incremental nodal force $\boldsymbol{\Delta F}$ can be expressed from micro to meso level by

$$\begin{Bmatrix}F^{int}_{Cx(J+1)}\\ F^{int}_{Cy(J+1)}\end{Bmatrix}_{[2\times 1]} = [\mathbf{1}_x \quad \mathbf{1}_y]_{[n_{ep}\times 2]}\, \boldsymbol{\Delta F}_{[n_{ep}\times 1]} \tag{35}$$

1.5.3 P-Δ Effect Consideration in Three-stage Analysis

In view of the importance of P-Δ effect [21] in structural engineering, the geometric stiffness matrix is added to the global tangent stiffness matrix at the macro level when the $\boldsymbol{k}_{[3N\times 3N]}$ in equation (28) has been constructed, the matrix is

$$\boldsymbol{k}_j = \boldsymbol{k}_j + \frac{P_j}{L_j}\begin{bmatrix} 1 & -1 & 0 & & & \\ -1 & 1 & 0 & & \mathbf{0} & \\ 0 & 0 & 0 & & & \\ & & & 1 & -1 & 0 \\ & \mathbf{0} & & -1 & 1 & 0 \\ & & & 0 & 0 & 0 \end{bmatrix} \tag{36}$$

where $\boldsymbol{k}_j$ corresponds to the part of global stiffness between the j th and (j + 1) th floors, P_j is the total axial force of the floor, and L_j is the story height.

1.5.4 Parallel Computing Algorism

To update the concurrent state of all floors of a building with sufficient accuracy, the message-passing interface (MPI) "grouping" technology is used in VEEL. Depending on the size of the structure, one VEEL runs on many central processing units (CPUs). The global master can concurrently harness multiple VEELs and perform the meso- and macro-level analyses with operating on a single CPU. Normally, the initial set of total CPUs called *MPI_COMM_WORLD* is a kind of the global set (Ω) consisting of total processors (p); $p = n(\Omega)$. The frame of the *MPI_COMM_WORLD* is shown in Figure 6. The global set splits subsets Ω_i with a small number of processors p_i and separate input/output flow. It can be represented as follows:

$$\Omega_i \subset \Omega \ \text{ for } \ i \in [1, N] \ \text{ and } p = \sum_{i=1}^{N} n(\Omega_i) \tag{37}$$

where N stands for the number of total subsets. In this case, N is equal to the number of total floors, and N floors are analyzed by N VEELs simultaneously. In the simulation, the degree of the nonlinearity among floors will be different since the concentrated damage would happen on the lower floors, only lower floors need to be analyzed by using VEEL. To solve the intergroup load imbalance, the total CPUs need be non-uniform decomposed. The detailed decomposition is shown below:

$$\begin{cases} n(\Omega_i) = n(\Omega_j) \text{ for } i \neq j & \text{uniform decomposition} \\ n(\Omega_i) > n(\Omega_j) \text{ for } i < j & \text{non} - \text{unifrom decomposition} \end{cases} \tag{38}$$

where *i* and *j* are floor numbers. The number of CPUs is assigned to the lower floor *i* increases with the structural components on a lower floor *i* that undergo nonlinear damage. Meanwhile, a coarse-grained algorithm which is good at the multiscale analysis [22] is adopted in the simulation. This algorithm allows each group consisting of a local master which can spawn sufficient slaves for parallel computations and communicates with the global master and its slaves that communicate only with the local master.

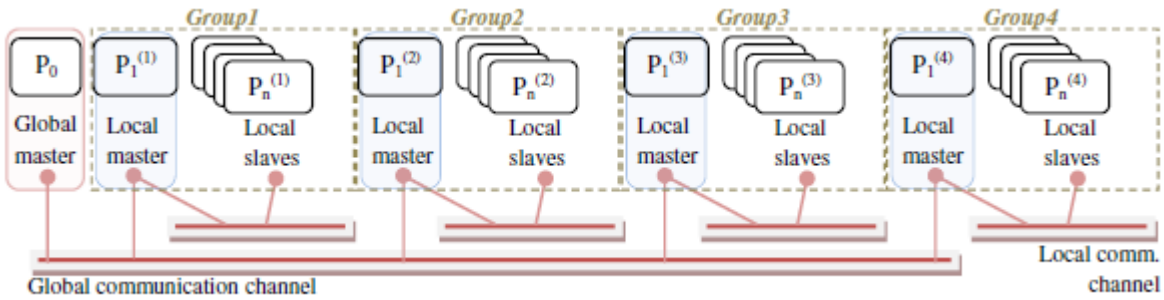

Figure 6. *Schematic illustration of the developed multiscale parallel analysis platform using the coarse-grained parallelization scheme and the MPI grouping technique (Cited from [18])*

CHAPTER 2. PRE-POST PROCESS OF THE VEEL

2.1 Preparation of three stage multiscale model

For doing the preprocessing of VEEL, the General Wall Preprocessing Program needs be installed, and the template input file need be prepared.

The content of the template input file includes:

- Number of longitudinal reinforcement group
- Number of stirrup group
- Number of horizontal reinforcement group along the Y axis
- Number of horizontal reinforcement group along the X axis
- The height of the wall and the top slab
- Length of the opening in the Z direction
- Length of the opening in the Y direction
- Length of the opening from the origin to the closest corner of the opening in the Y direction
- Length of the opening from the origin to the closest corner of the opening in the Z direction
- Material solid ID
- Number of rectangular concrete blocks (whose order is the left corner, then the right order)
- Nodal force
- Nodal force direction (1 is x, 2 is y, 3 is z)
- Reference force direction (1 is x, 2 is y, 3 is z)

- Reference node height.

2.1.1 Building Information

For the longitudinal reinforcement of each group, there are a number of groups for a wall, the data will be listed with the following order and repeated for the number of the groups.

- Corner 1 (left corner) x coordinate
- Corner 1 (left corner) y coordinate
- Corner 2 (right corner) x coordinate
- Corner 2 (right corner) y coordinate
- Number of the longitudinal reinforcement in the x-direction
- Number of the longitudinal reinforcement in the y-direction
- The material ID for the longitudinal reinforcing steel
- Corner 1 (left corner) z coordinate
- Corner 2 (right corner) z coordinate

To define the stirrup group, the rule is the same as one of longitudinal reinforcement data. However, the layout is following the below sequence:

- Corner 1 (left corner) x coordinate
- Corner 1 (left corner) y coordinate
- Corner 1 (left corner) z coordinate
- Corner 2 (right corner) x coordinate
- Corner 2 (right corner) y coordinate
- Corner 2 (right corner) z coordinate

- Number of stirrups in the z-direction
- The material ID for the stirrup reinforcing steel

For defining the horizontal reinforcement of each group, the rule is the same as the above, the sequence is:

- Corner 1 (left corner) x coordinate
- Corner 1 (left corner) y coordinate
- Corner 1 (left corner) z coordinate
- Corner 2 (right corner) x coordinate
- Corner 2 (right corner) y coordinate
- Corner 2 (right corner) z coordinate
- Number of the reinforcing steel in the x-direction for wall parallel with y-axis, in the y-direction for the wall parallel with x-axis
- Number of the reinforcing steel in the z-direction for

After the template input file is generated, the formal and complete VEEL input file would be prepared. It is the input data for parallel computation of the shear wall finite element analysis on condo super-computer cluster, which contains all the required information for the analysis. Besides the data prepared in the template input file, the other data is prepared by General Wall Preprocessing Program. The information is divided in the following portions:

1. Project information

The project information presents overall information about the target wall. The symbol "%" indicates the comment which typically includes analysis description, reference,

data, authors, important parameter changes and other user notes for the analysis. The lines after "INPUT INFORMATION" are an input summary of the analysis. The input information includes node, element, surface force, nodal force, nodal reference force, specified displacement, fixed boundary, material, hysteresis, integration, output, displacement history data, and perfectly bounded steel, which needs to be consistent for the entire document.

2. Coordinate

Each node has a three-dimension coordinate (x, y, z). The sequence of the coordinate is from the smallest to the largest value of the x coordinate, then the ones of the y coordinate, the last one is the ones of the z coordinate. The coordinate of one node is shown below:

Node number	Coordinate x	Coordinate y	Coordinate z
1	0.00000000e+00	0.00000000e+00	0.00000000e+00

3. Boundary condition

All the nodes at the bottom have zero in the z coordinate, which defines the bottom nodes have a fixed boundary condition. There are two options for boundary conditions. Value "1" represents fixed boundary condition, and value "0" stands for free boundary condition. The boundary condition example is shown as follows:

Node number	Boundary Condition x	Boundary Condition y	Boundary Condition z
1	1	1	1

4. Nodal Force

The applied vertical loads on the specific nodes are used to simulate compression loads on the wall. The nodal force can be expressed as follow:

$$nodal\ force = F/n$$

where *F* is the vertical force, *n* is the number of the total nodes in the horizontal section of the wall. The vertical force can be calculated by:

$$F = ratio \times P = ratio \times f_c' \times A_g$$

where the ratio is axial force ratio ($ratio = F/P$), P is the concrete compression capacity ($P = f_c' A_g$). f_c' is concrete yielding strength and A_g is the cross-section area of the wall. The nodal force in x, y, z direction defines the load direction and the load value. The "-" sign means the load in the reverse direction of the position axis direction.

Node number	Nodal Force x	Nodal Force y	Nodal Force z
55441	0.00E+00	0.00E+00	-4.43E+05

5. Nodal reference force

Nodal reference force defines the directions of the displacement for the displacement history data section. In the following example, the "1" defines in x-direction for node number 30 means that the primary displacement direction in x-direction. The "2" defines in y-direction for node number 15 means that the secondary displacement direction is in y-direction. There are only two (i.e. primary and secondary) directions

available in the program. Note that the first line of the displacement history defines a node and a direction. The example of nodal reference force is represented below:

Node number	Disp. Direction x	Disp. Direction y	Disp. Direction z
30	1.00	0.00	0.00
15	0.00	2.00	0.00

6. Material

The material properties are defined through parameters in column A, B, C, D, E and F. The "A" represents material identification (ID); the "B" represents Young's modulus (N/m^2 or Pa); the "C" represents Poisson's ratio; the "D" represents material weight (kg/m^3); the "E" is the temperature coefficient; the "F" is hysteresis model identification. The example of the material is listed below:

A	B	C	D	E	F
1	1.31E+8	0.2	2402.77	0.23	1
2	20E+10	0.3	0.0	0.3	2

7. Hysteresis

There are five concrete and three steel hysteresis model options. The hysteresis models vary from simple linear to complex nonlinear properties. The number of the type and the name of the hysteresis model are shown below.

Type no. Name of the hysteresis model

10 Linear Elastic

11 Thorenfeldt Concrete Model

12 Modified Thorenfeldt Concrete Model

13 Confinement Dependent Modified Thorenfeldt Concrete Model

14 Nonlocal-information based Confinement Modified Thorenfeldt Concrete Model

21 Bilinear Steel Model

10001 Bilinear Steel Model with Compressive Buckling

10002 Menegotto-Pinto Steel Model with Compressive Buckling

The hysteresis number is the same as the material identification. The input parameters for the different type of hysteresis models are shown below.

Hysteresis no.	Type no.	Input parameters
1	10	0
2	11	f_c' ε_c f_t ε_t ε_u
3	12	f_c' ε_c f_t ε_t ε_u c
4	13	f_c' ε_c f_t ε_t ε_u c
5	14	f_c' ε_c f_t ε_t ε_u c
6	21	A_s σ_y ε_y c_0 (σ_u)
7	10001	A_s σ_y ε_y c_0 σ_u c_1 c_2
8	10002	A_s σ_y ε_y b σ_u c_1 c_2

where f_c' is concrete compressive strength whose unit is Pa; ε_c is a strain at the compressive strength; f_t is tensile strength whose unit is Pa; ε_t is a strain at the tensile strength; ε_u is an ultimate tensile strain; c is coefficient to determine softening shape, which has a range is from 0.31 to 1.0; $A_s$is an area of steel; σ_y is yielding stress; ε_y is strain at the yielding stress; c_0 defined by post yield young's modulus over initial young's modulus; σ_u is the ultimate tensile stress; $c_1$is the reduction factor for post-buckling, softening regime; c_2 is the factor for residual strength after buckling; b is the reduction factor for post-yielding, hardening response.

8. Connectivity

Connectivity defines the cube element and material of the element. The example of connectivity is shown below:

Element no.	Material ID	Eight nodes of the cube element							
1	1	1	2	48	47	694	695	741	740
97638	7	55434	55435	55275	55274	56127	56128	55968	55967

9. Perfectly bounded steel

Each reinforcing bar is modeled by a space truss element. A space truss element consists of two end nodes. An example of a perfectly bonded steel is shown below.

Truss element number	Material ID	Node 1	Node2
1	2	48	741

10. Displacement history

Displacement history data is obtained directly from a paper or extracted from the displacement figures in a paper. The genuine target is to find the peak displacement points. Then, refine the displacement load steps by adding additional points between the peak points. The first line in the displacement history data defines the node number and the displacement direction (1, 2 and 3 are for x, y and z directions respectively). This node number is one of the nodes in the defined nodal reference force group. The defined displacement history data following the first line is for the entire nodal reference group. The direction of the displacement should be consistent. The first line of the primary displacement history data should be in the same direction of the primary nodal reference force group. Both are defined in x-direction. Both secondary displacement history data and nodal reference group should be defined in the same y-direction. The "A" is node number; the "B' is displacement direction; the "C" is displacement load step number; the "D" is displacement value. The example for primary and secondary displacement history data is shown below:

Displacement History (Primary)
56613^{A} 1^{B}
1^{C} $0.00E+00^{D}$
. .
. .
. .
Displacement History (Secondary)
48151^{A} 1^{B}
1^{C} $0.00E+00^{D}$
. .
. .
. .

11. Nonlinear control data

The nonlinear control data provides another refinement option for the displacement of load steps and control data for the incremental-iterative solution procedure. The “A” is the total number of load time steps times of the total displacement load time steps, the total number of load time steps is an integer number; The “B” is the maximum iterations per time step; The “C” is the maximum iterations per displacement control; The “D” is an internal debugging setting which must be zero. The definition of the nonlinear control data is explained respectively below.

A	B	C	D
992	50	3	0

12. Newton Raphson tolerance

The Newton Raphson method is a technique used to find the roots of nonlinear algebraic equations. The “A” is force norm that is the Euclidean norm of the out-of-balance force vector. The “B” is displacement norm that is the Euclidean norm of the iterative displacement increment. The example of Newton Raphson tolerance is shown below:

A	B
1.0000e-03	1.0000e-03

The complete and short version of the input file is shown in Appendix A.

2.1.2 One-direction Ground Excitation

Besides the input file described above, the ground motion information is another important input for the simulation. The ground motion information is obtained from the Pacific Earthquake Engineering Research (PEER) Ground Motion Database [23]. From the existed eleven databases, the one is scaled by 3.1838 since peak ground acceleration is highest that is about 0.8g is selected to simulate the extreme situation. Since the key point of RCSW building is the development of inelastic behavior from beginning to emerge, the range of the selected ground acceleration is shown below.

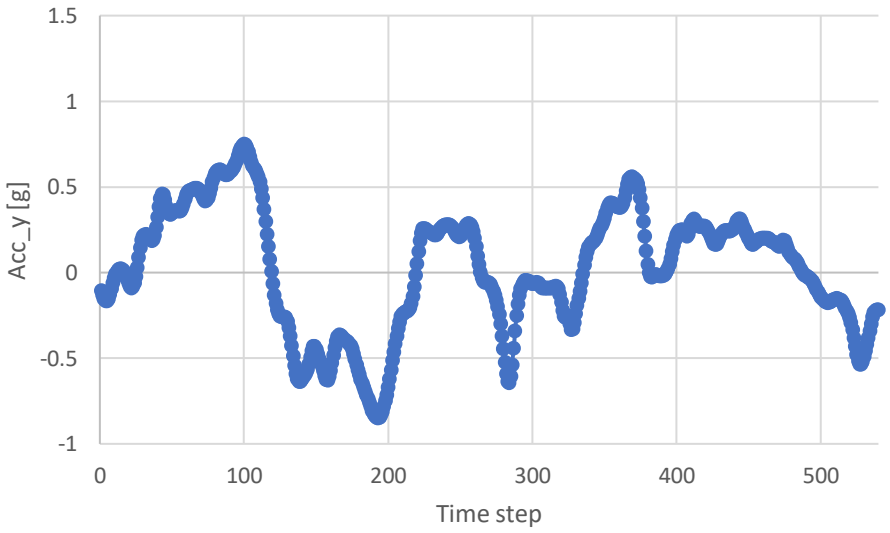

Figure 7. *Ground Motion Acceleration*

The Pseudo-acceleration response spectrum (Figure 8) and the Pseudo-displacement spectrum (Figure 9) are generated by the scaled-up ground acceleration which is shown in Figure 7. The shaded box in figure 8 and 9 show the range of the natural vibration periods of the four target buildings. The four lines in the shaded area are represented for the first mode of four buildings which are separately 0.12776sec, 0.139798sec, 0.242787sec, 0.418313sec. With

the height and number of story increase, the first mode of natural vibration period and the related range increase correspondingly. It should be noted that we restrict our focus on the relatively early phase at which inelastic behavior of the RCSW building begins to develop, not on the complete collapse state.

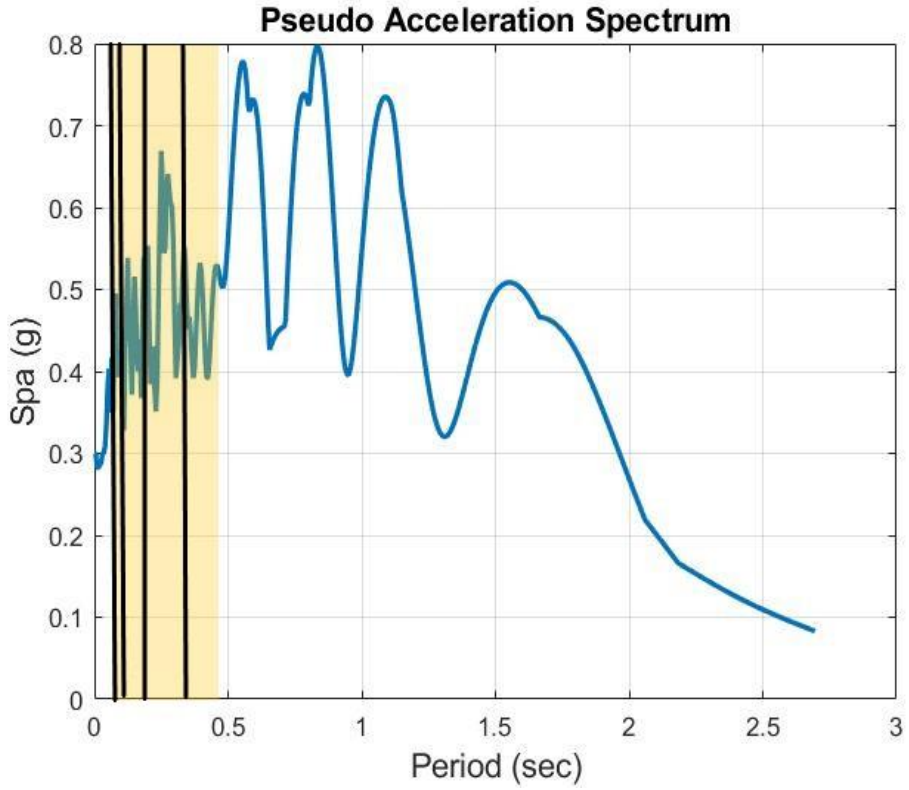

Figure 8. *Pseudo Acceleration Spectrum*

After preparing the required input file, they were uploaded to the Virtual Earthquake Engineering Laboratory(VEEL) which is on the Condo supercomputer, the VEEL would simulate the building prepared before under the earthquake motion which we selected by ground motion information. The result from the VEEL need be analyzed by post analysis programs.

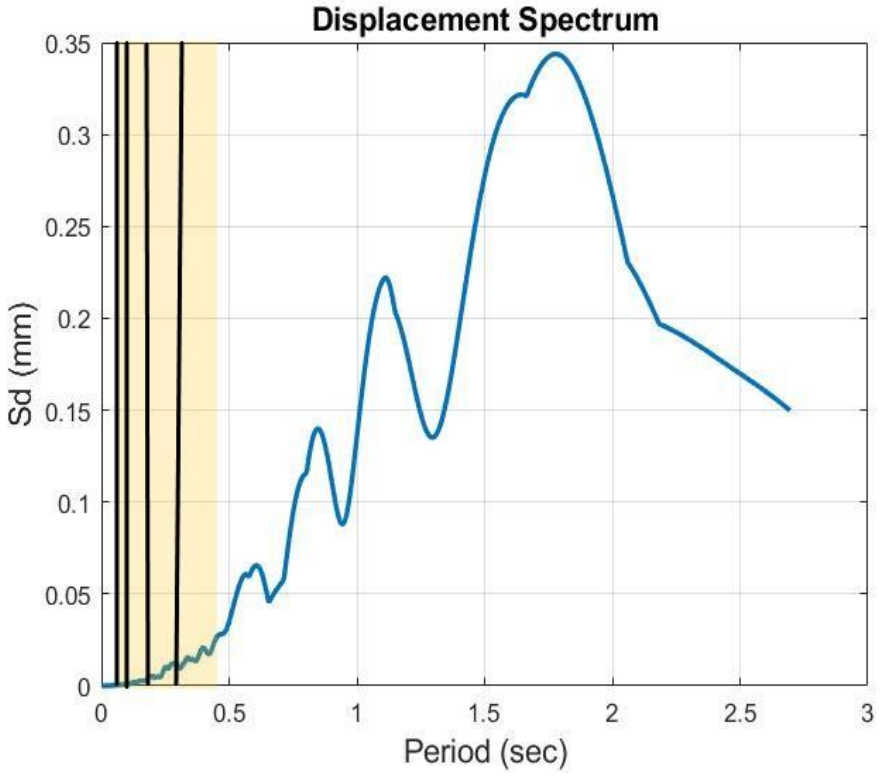

Figure 9. *Pseudo Displacement Spectrum*

2.2 Post-process analysis of the simulation from the VEEL

After the analysis of the VEEL, the simulation data of building with the development of time and ground excitation were captured. To make it meaningful, two analysis programs that are Post_THA and Post_TSC were used, which is created in Matlab, they are utilized to analyze the macro level and micro level building information.

In Post_TSC program, there are several settings to do the varied analysis in micro-level. Some of the setting was used in this research will be described as following:

Setting 1: Nodal reference force vs. Nodal displacement

The result of this setting helps to obtain the force and displacement acted on the structure with the time step and ground motion developing. At the same time, it can also

show the relationship between force and displacement. The operation of the setting is listed below:

- Insert the result of the simulation from the VEEL;
- Select the option of nodal reference force vs. nodal displacement;
- Select the interested reference force, there are primary and secondary two options;
- Run the program for analyzing;

Setting 2: Steel stress vs. strain

The result of the setting shows the stress and strain of indicating steel bar in the interested structure. It can be used for later analysis, such as steel strain contour plot, the relationship between strain and stress for all indicator bar and so on, which is helpful to easily identify the condition of steel with the time and ground motion increasing. The operation of the setting is shown below:

- Insert the result of the simulation from the VEEL;
- Select the option of steel strain vs. strain;
- Define the number of indicator steel;
- Define the interested plane of the interested wall, there are two options that are x-z and y-z;
- List the coordinate of the indicator steel;

- Run the program for analyzing;

Setting 3: At a specific time, capture steel related information

The result of the setting shows all related information about steel bar at a specific time. The specific time may be beginning or end of the earthquake. The steel related information includes the node id about the steel bar which included top node j and bottom node i, strain and stress of the steel bar, length of buckling and index of buckling condition. The result can be used for later analysis which is plotting the progressive bar buckling. The operation of the setting is shown below:

- Insert the result of the simulation from the VEEL;
- Select the option of steel-related information at a specific time;
- Define the time step interested;
- Define the number of indicator steel about the interested wall;
- Run the program for analyzing;

In Post_THA program, only one setting was used in my study will be described as following:

This setting is used to capture resisting force and displacement at the macro-level with the time step and ground motion developing. At the same time, it can also show the relationship between force and displacement in macro-level. The operation of the setting is listed below:

- Insert the result of the simulation from the CONDO;
- Select the option of nodal reference force vs. nodal displacement;
- Select the interested reference force, there are primary and secondary two options;
- Select the interested node of the building, there is a floor between adjacent nodes;
- Run the program for analyzing;

The sample result of the post-process analysis program listed in Appendix B.

CHAPTER 3. MODELING THE STUDY BUILDINGS

3.1 The Target Buildings Information

This study focuses on four typical 1970's RCSW buildings with the identical structural layout on each floor. To investigate the impact height on the complex reinforced concrete shear walls under the extreme earthquake, four target buildings are separately 4 stories, 8 stories, 12 stories, and 16 stories. The first floor is garage floor that is under the ground. The height of the second floor is 4.83 m and one of the other floors is 4.47 m, which causes an irregular situation on the second floor. The damage may be serious on the second floor. Figure 10 is briefly shown the target buildings information.

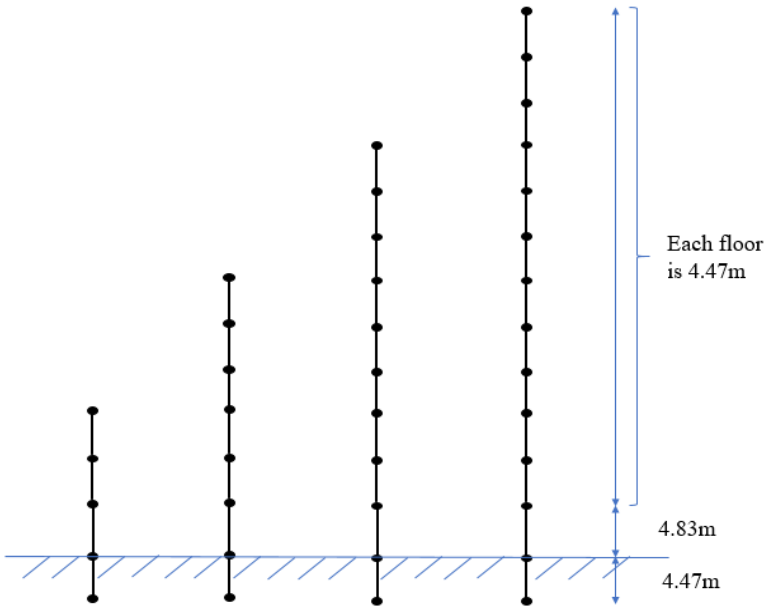

Figure 10. *Four target buildings with vertical irregularity.*

Each floor of these four building has the same layout that is one box-shaped wall with an opening, one rectangular wall and two L-shaped walls (Figure 11) to simulate complex geometry. There are also twenty-seven reinforcement concrete columns in each floor. These

four buildings are similar to an actual building located in the California region and designed based on 1970's building code, the floor mass is 551,114.7 kg. The box-shaped wall contains No. 5 horizontal and vertical bar grid. The concrete cover is 0.051 m thick. The web and flanges of L-shaped walls contain with No. 6 horizontal and vertical bar grid. The rectangular wall is 0.61 m and contains No. 5 horizontal and vertical bar grid. The horizontal and vertical spacing of the bar grid on the wall systems is 0.2794 m and 0.4572 m. The dimension of exterior columns is 0.686 m x 0.686 m and reinforced by eight longitudinal bars that are No. 14 bars, and No. 4 stirrups spaced at 0.1 m. The Interior columns have four longitudinal bars (No. 11) and the same stirrups as the exterior ones. All concrete cover is 0.051 m thick. All structural elements used herein are assigned with the concrete strength (32.44 MPa at ε = 0.002) and the steel yield strength (420 MPa at ε = 0.0021). The concrete hysteresis model used herein is Modified Thorenfeldt Concrete Model with Nonlocal-information-based Confinement Model and the steel hysteresis model used is Menegotto-Pinto Steel Model. Both material models are introduced in chapter 1.4.

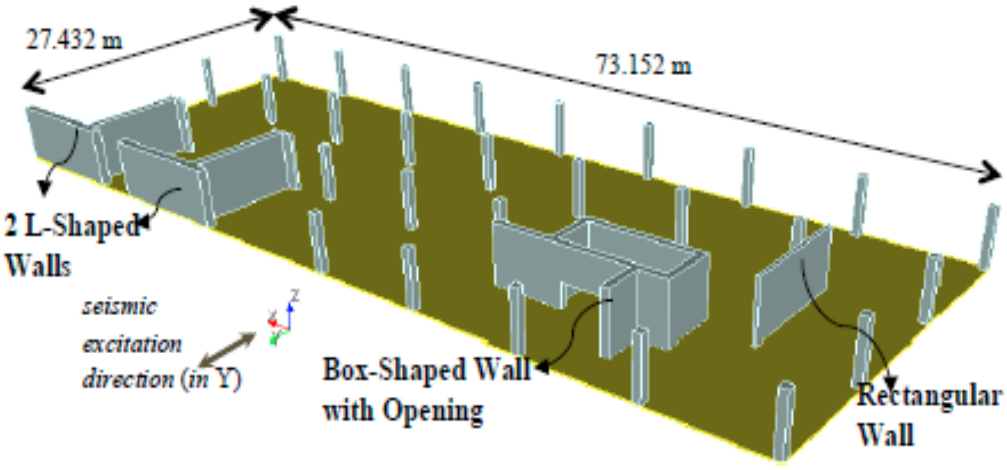

Figure 11. *Each floor layout for target buildings*

3.2 Multiscale Response of RCSW Buildings

The result of simulation offers a valuable access to multiple length scales 'damage responses of the RCSW buildings. This section presents fully coupled dynamic responses from building-, soft story-, and core wall-level (i.e. macro-, meso- and micro-level) and draws important implications at each scale.

3.2.1 Building-Level (Macro-Level) Responses

Uni-directional ground excitation results in multi-direction damage in a complex wall, which is a kind of unexpected behavior of the RCSW building. Particularly, the core wall has the irregular layout and an opening, which may cause bi-directional motions under the multi-directional loading uniaxial ground excitation. Severe damages on a portion of a complex wall directly can result in stiffness degradation in other directions.

Inter-story drift ratio (ISDR) is an important damage demand parameter to estimate the response quantity and indicator of structural performance in seismic analysis, which is used to monitor building-level damage. The expression of calculation of inter-story drift ratio is listed below:

$$IDSR_i(t) = \frac{|d_i(t) - d_{i+1}(t)|}{h_i} \tag{39}$$

where $d_i(t)$ means the displacement of the node i at time t, h_i represents the height of the story i. The all-time maximum value of inter-story drift ratio ($\overline{IDSR}$) is reasonable to indicate the behavior of building for better understanding the shear displacement loading imposed on the primary shear walls during the dynamic excitation. the expression is

$$\overline{IDSR_i} = \max_{in\ \forall\ t}[IDSR_i(t)] \tag{40}$$

For the torsion, the inter-story torsional angle (ISTA) is used to measure all-time inter-story angular rotation and defined as:

$$\overline{ISTA_i} = \max_{in\ \forall\ t}[|\theta_i(t) - \theta_{i+1}(t)|] \quad (41)$$

where $\theta_i(t)$ is angular rotation about the Z axis of the node i at time t

The point of the inter-story drift is corresponding to each floor in four target buildings in the following figures, which is calculated by the difference of the inter-story drift of two nodes. One story is between two adjacent nodes. Based on the multiscale dynamic result of four RCSW buildings, the different distributions of $\overline{IDSR}$ is present in the following figures.

Since the buildings with the vertical irregularity, the second floor is a slight "soft" floor. Even if the ratio is small, it is clear to show that the nonlinear damage is severely concentrated on the soft story. No matter the height changes, the maximum value of the inter-story drift exists in second floor normally and the larger ratio usually happens in lower floors. With the number of floor increases, the value will decrease. Comparing Figure 12 and 13, the IDSR in primary direction is larger than the one in secondary direction for the same building, it elucidates the primary direction wall did major contribution of the box-shaped wall. The torsion happened in four buildings shown in Figure 14 is not serious and only lower four floor has a relative large ratio. The concentration of the induced torsional rotations on the soft second floor is exacerbated for taller buildings. The buildings should enhance the resisting for the displacements in the primary direction and the torsion in the lower floor.

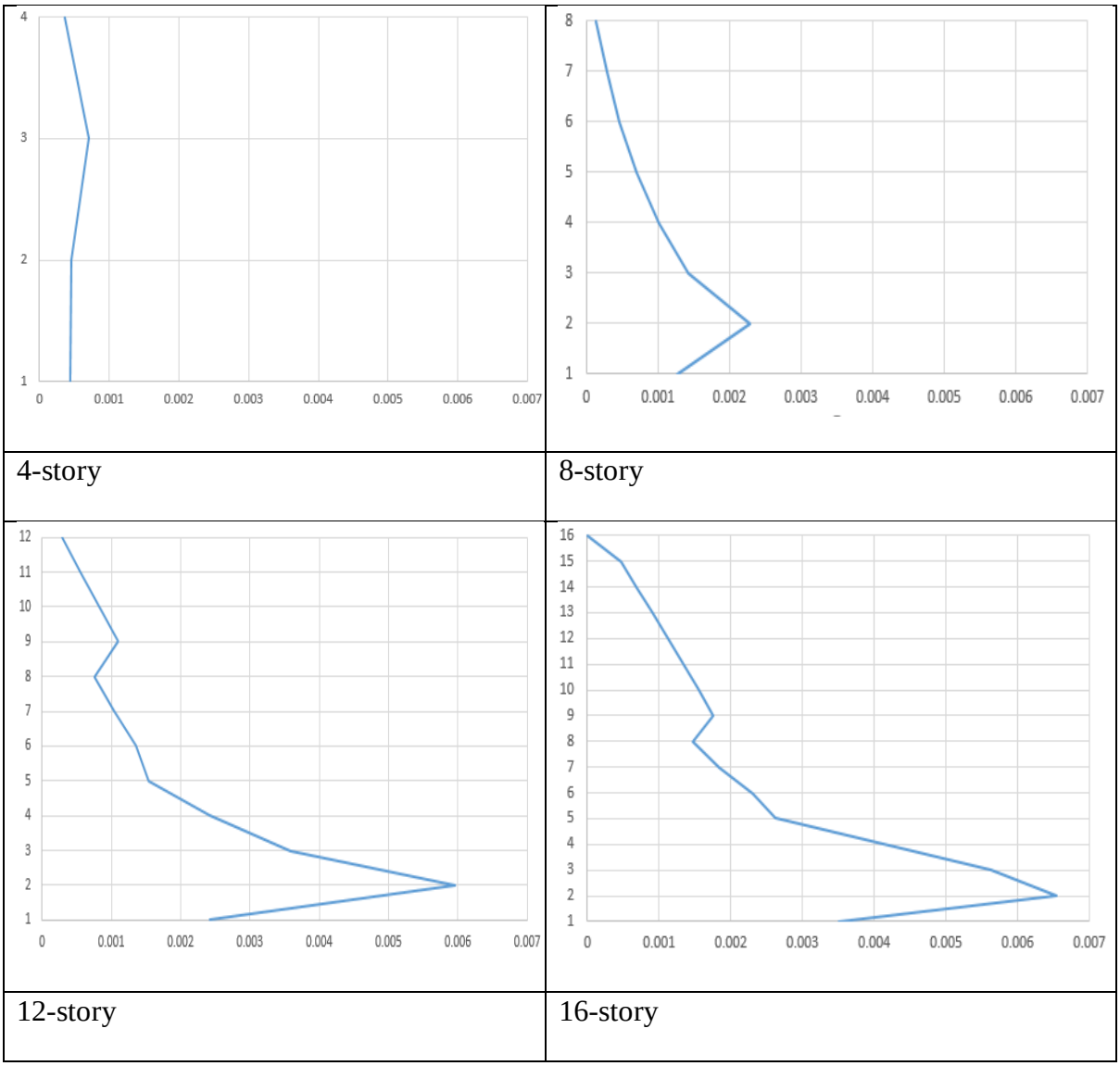

4-story | 8-story

12-story | 16-story

Figure 12. *The all-time inter-story drift ratio of the four target buildings in the primary direction*

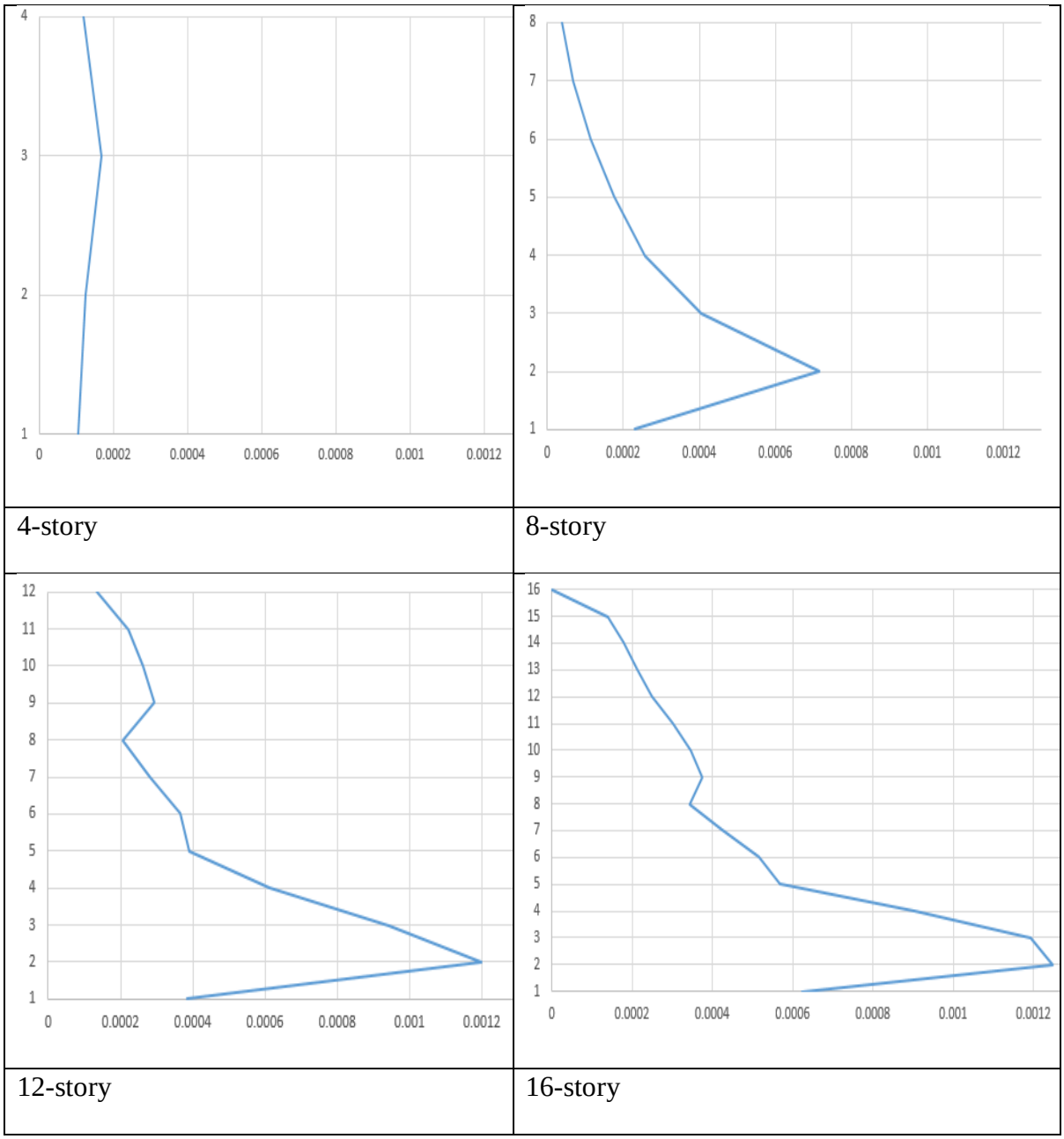

4-story | 8-story

12-story | 16-story

Figure 13. *The all-time inter-story drift ratio of the four target buildings in the secondary direction*

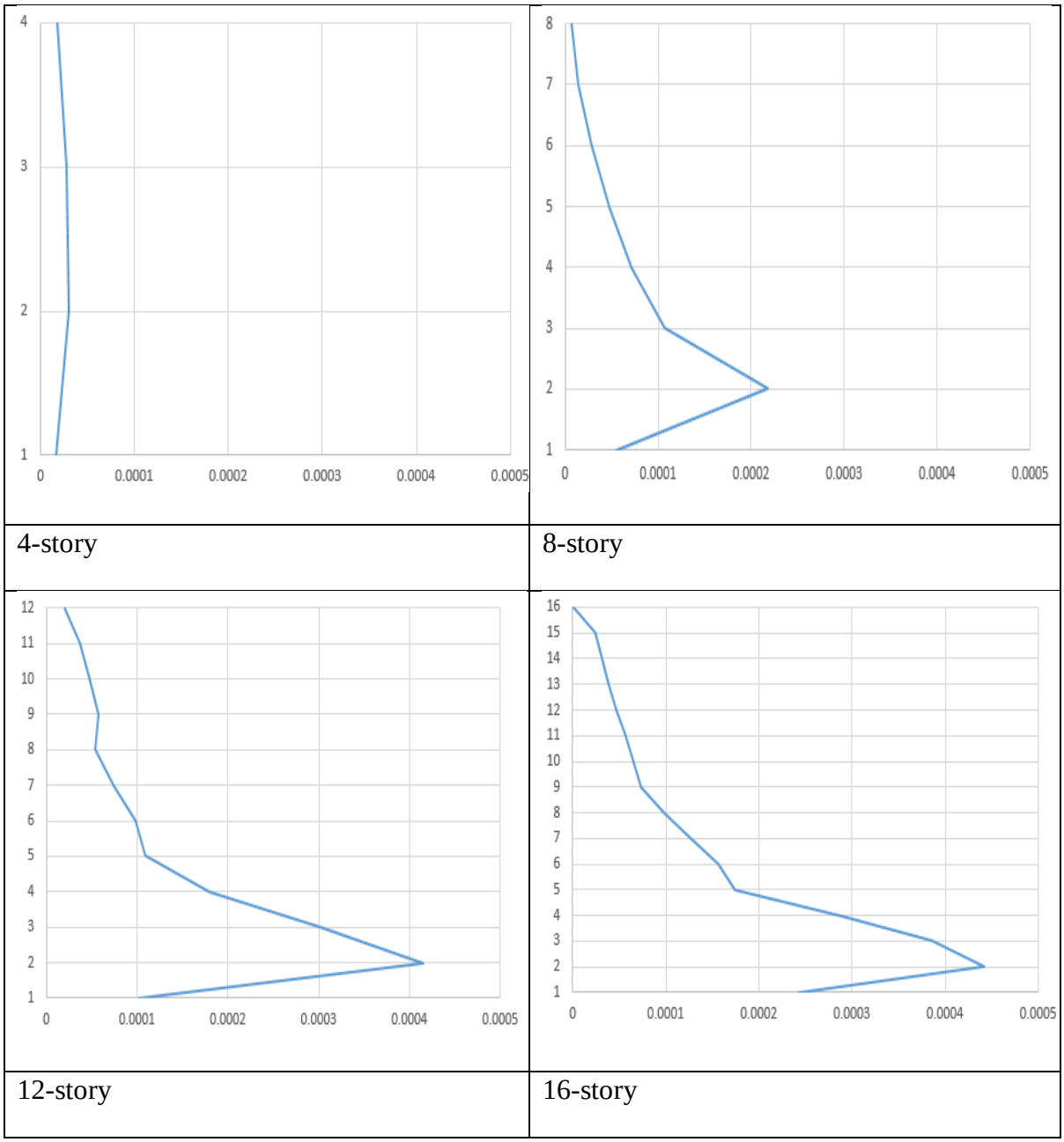

4-story | 8-story

12-story | 16-story

Figure 14. *The all-time inter-story torsional angles of the four target buildings for torsion.*

3.2.2 Floor-Level (Meso-Level) Responses

As damages on core walls are gradually aggravated by dynamic excitation, floor-wide shear force redistribution among wall systems naturally take place. The relative shear force ratio of each wall on an RCSW system on a floor is defined as

$$\left|F_y^{(i)}(t)\right| / \sum_{i=1}^{NW} max\left|F_y^{(i)}(t)\right| \tag{42}$$

where $F_y^{(i)}(t)$ is total shear force carried out by *i* th shear wall which is obtained from either the macroscopic multi-linear model or the micro-level multiscale FEA of the *i* th wall system., t means time step, NW stands for the total number of the primary-direction walls on a floor (herein NW=3).

In the target buildings, each floor includes a box-shaped wall, two L-shaped walls, and a rectangular wall. For ease in comparing relative shear forces, the shear force ratio of Box-, L-, and the rectangular wall of the second floor in the four target RCSW buildings is normalized.

The 4-story RCSW building did not happen non-linear damage shown in Figure 15. From the figure, the shear force redistribution of the Box-shaped wall is higher than other walls that means the Box-shaped wall is mainly contribution of the resisting system throughout all time steps. Even if the L-shaped walls are far away from the Box-shaped wall and Rectangular wall, the L-shaped walls are the second position of the contribution of shear force for the resisting system. The rectangular wall is the less contribution than the Box- and L-shaped walls.

In the second floor of the 8-story building, the Box-shaped wall is still a largest contribution of shear force before the time step 220 which the vertical red line is located shown

in Figure 16. On the right side of the vertical red line, the L-shaped wall takes the largest contribution position and takes place of the Box-shaped wall. The rectangular wall is still the smallest contribution of the resisting system. With the height of the building increase, the damage of the box-shaped wall accumulated.

In Figure 17, it shows the shear force redistribution of the second floor of the 12-story RCSW building. The contribution role of the box-shaped wall is transferred to the L-shaped wall around the time step 50 that is earlier than the situation in the 8-story building. That means the severe damage on the box-shaped wall happened around time step 50. The rectangular wall is still the smallest contribution of the resisting system.

In the 16-story RCSW building, the L-shaped wall takes over the role of primary shear-force resisting mechanism throughout nearly all-time steps in Figure18. The L-shaped walls' shear force exhibits larger contribution to the floor shear than the box-shaped wall. The damage of box-shaped wall happened from the beginning. Meanwhile, the rectangular wall is still the smallest contribution of the resisting system.

With the height of the target building increases, the damage of box-shaped wall happened earlier and more serious. At the same time, the L-shaped wall is becoming primary resisting mechanism from the secondary position. For higher buildings, more damage tends to concentrate on the primary box wall at the early stage, and thus the role of the next primary L-shaped wall becomes significant.

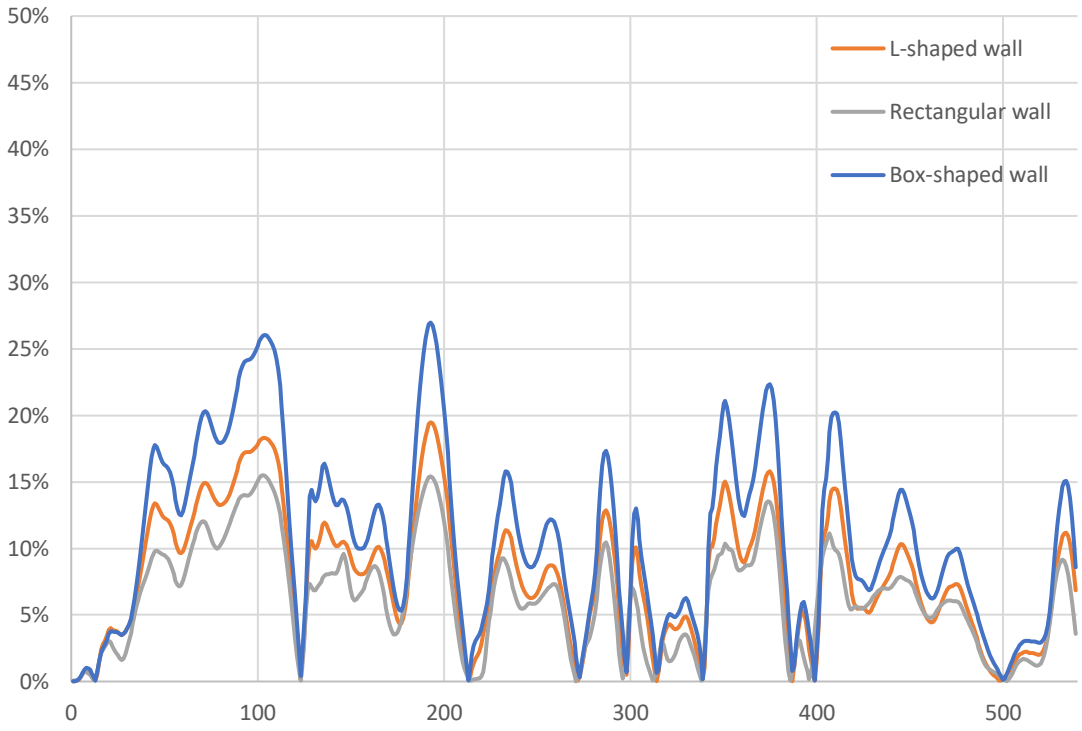

Figure 15. *The development of the shear force redistribution of box-shaped, L-shaped and rectangular walls on the second floor of the 4-story building with a time step developing and the trend of the shear force redistribution.*

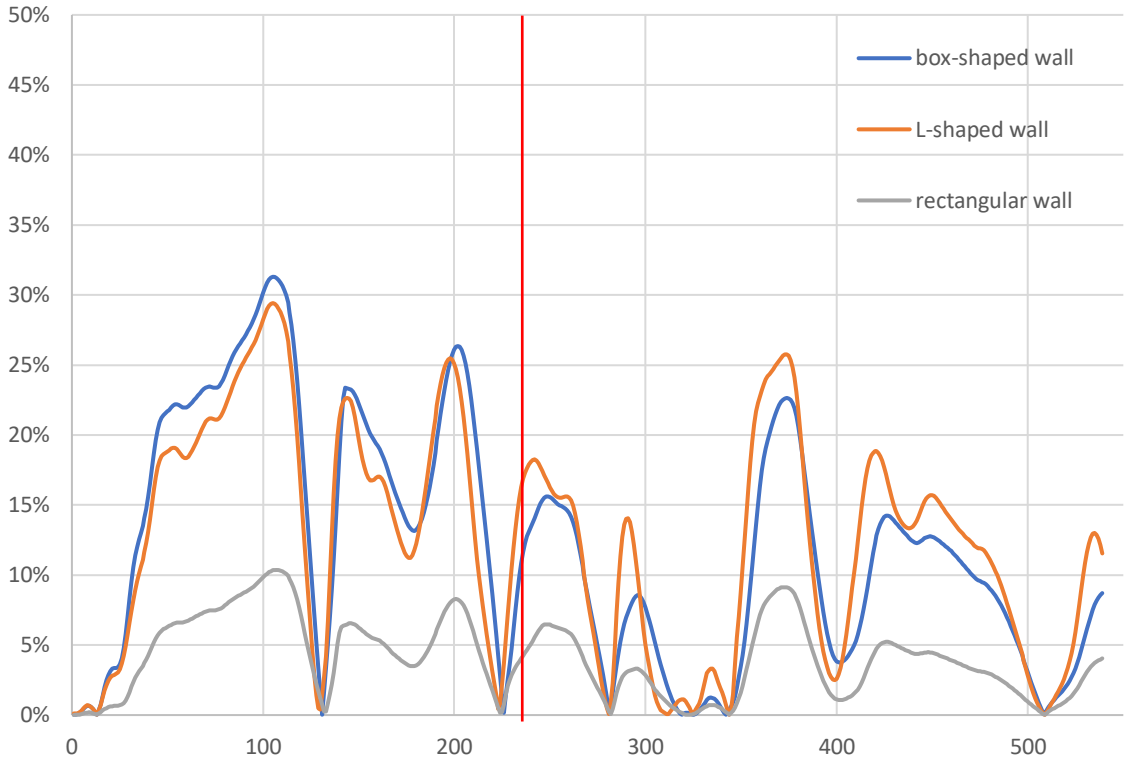

Figure 16. *The development of the shear force redistribution of box-shaped, L-shaped and rectangular walls on the second floor of the 8-story building with a time step developing and the trend of the shear force redistribution.*

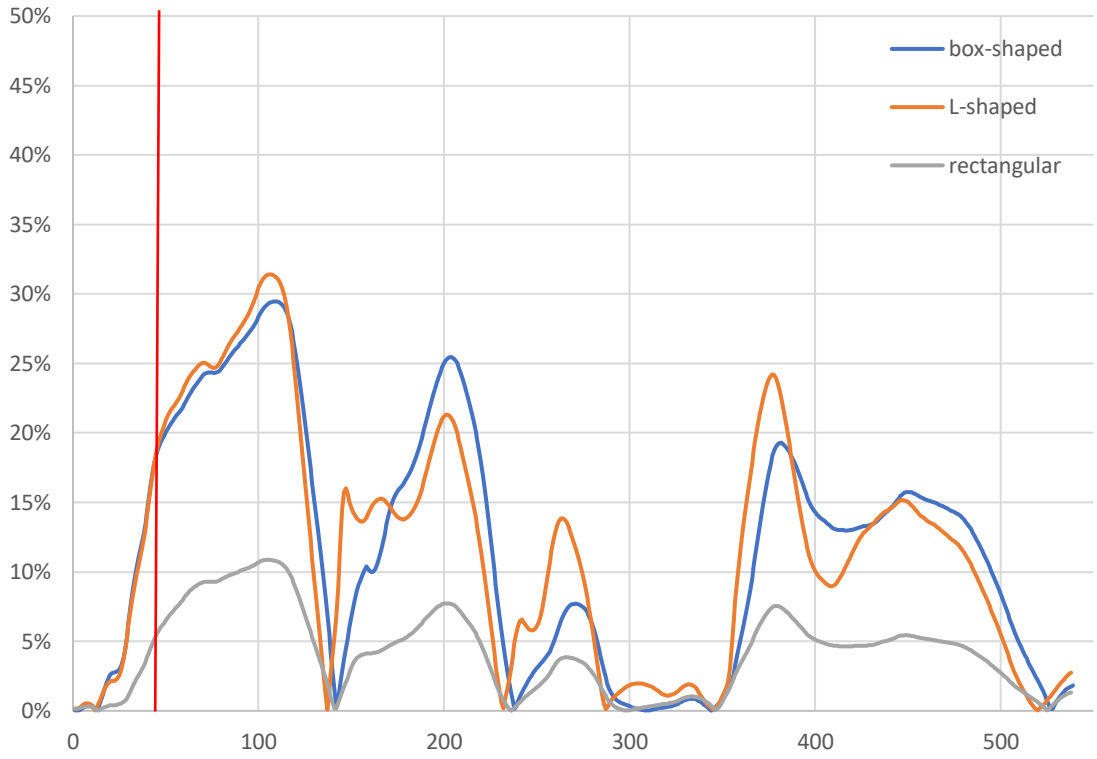

Figure 17. *The development of the shear force redistribution of box-shaped, L-shaped and rectangular walls on the second floor of the 12-story building with a time step developing and the trend of the shear force redistribution.*

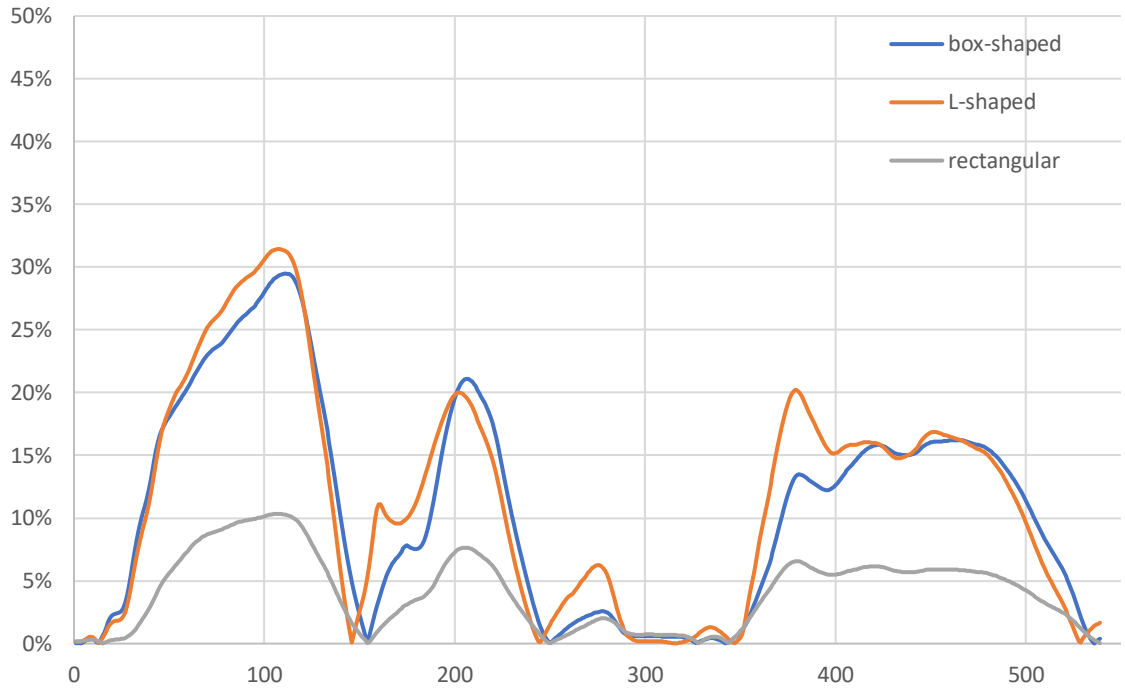

Figure 18. *The development of the shear force redistribution of box-shaped, L-shaped and rectangular walls on the second floor of the 16-story building with a time step developing and the trend of the shear force redistribution.*

3.2.3 Wall-Level (Micro-Level) Responses

Based on floor-level responses, the core box-shaped wall and L-shaped wall are worth to analyze in wall-level to find how the damage happened with various heights. The cumulative damage, such as concrete crushing and cracking as well as steel bar yielding, are irreversible degradation. The absolute maximum strains of each panel of the wall is a good way to monitor the cumulative damage stage. The cumulative strain contour plot of walls in the second floor was defined by about five-hundred-step of ground motion acceleration. The maximum tensile strain of bar can indicate the situation of bar yielding, and the minimum compressive strains can indicate concrete spalling or crushing.

First, the box-shaped wall was concerned since it takes largest shear force in lower buildings, which has two-direction panels which are xz-direction panel and yz-direction panel. The contour plots of the box-shaped wall in the second floor in four buildings were shown below.

From Figure 19(a), the concrete of the xz-panel of the box-shaped wall of the second floor in the 4-story building didn't happen crushing. The right bottom corner of xz-panel in the 8-story building has a little crushing shown in Figure 19(b). In the 12-story building, besides the crushing in both bottom corners in the panel, the right top corner also happened a little crushing shown in Figure 19(c). In Figure 19(d), the crushing area in the top right corner and bottom corners is gradually increasing and slightly larger than the total crushing area in the 12-story building. The red line marked the crushing area.

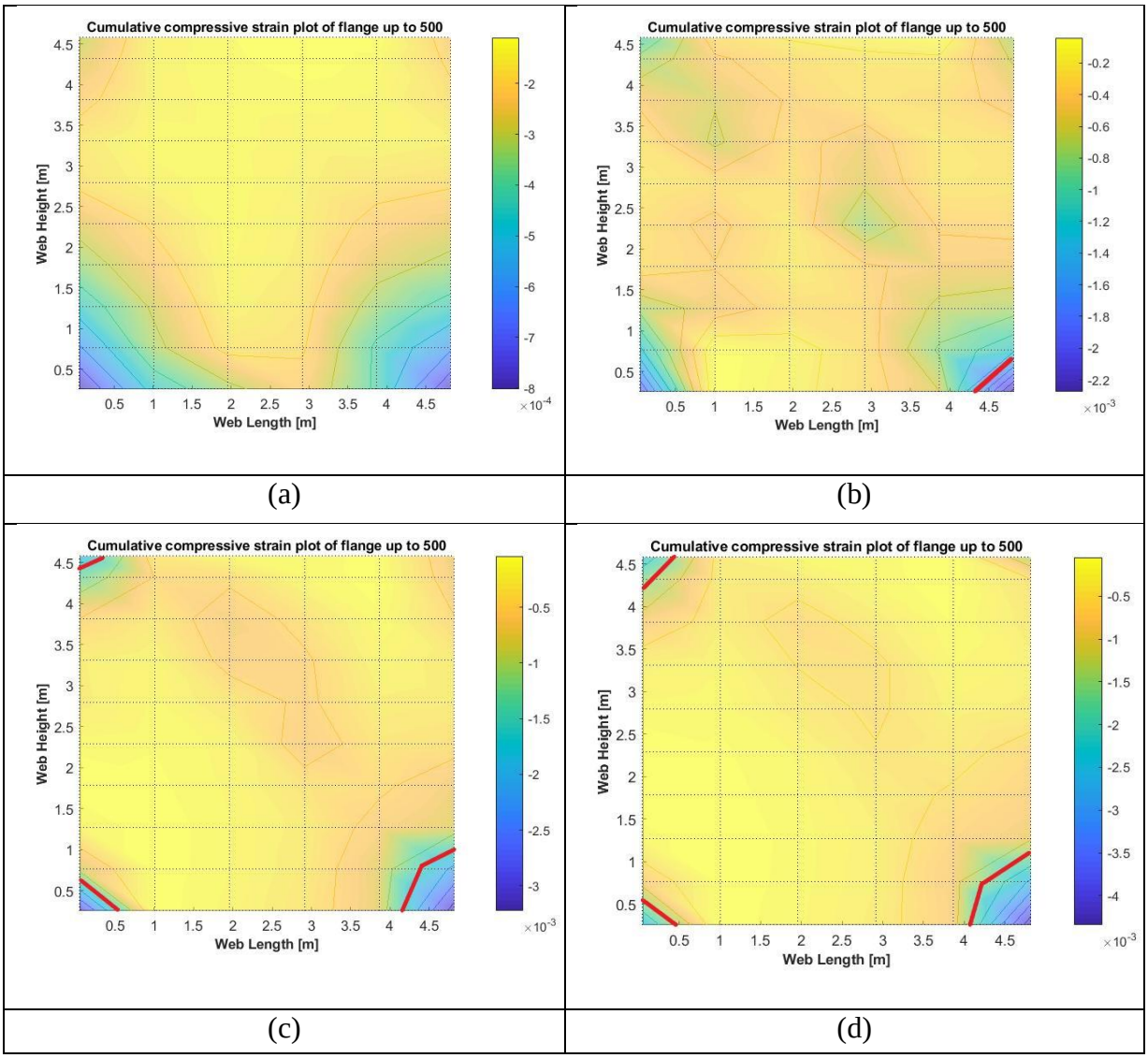

Figure 19. *Compressive contour plot of xz--panel in the second floor in the four buildings. (a) is 4-story building contour plot, (b) is 8-story building contour plot, (c) is 12-story building contour plot, (d) is 16-story building contour plot.*

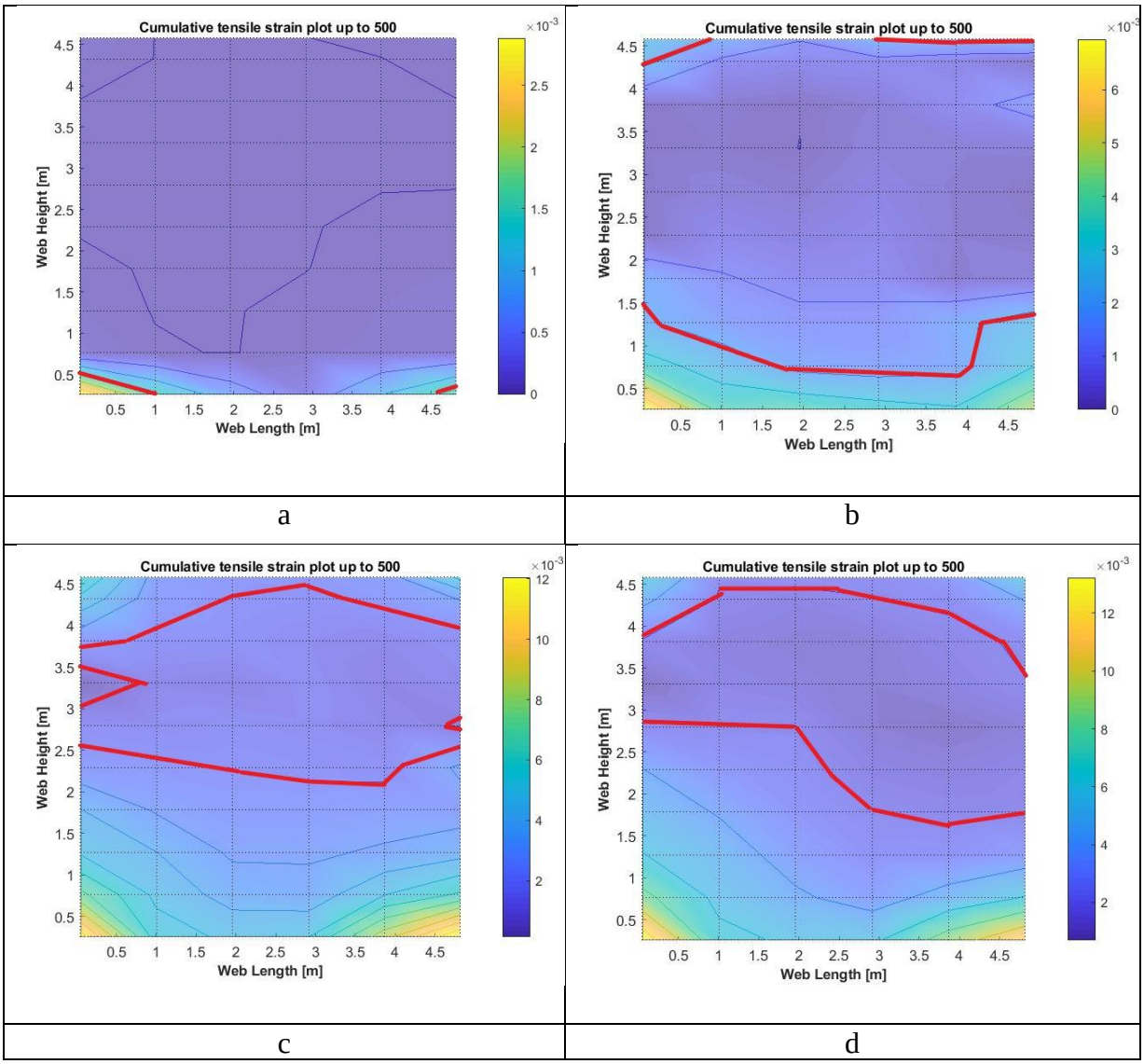

Figure 20. *Tensile contour plot of xz--panel in the second floor in the four buildings.is 4-story building contour plot, (b) is 8-story building contour plot, (c) is 12-story building contour plot, (d) is 16-story building contour plot.*

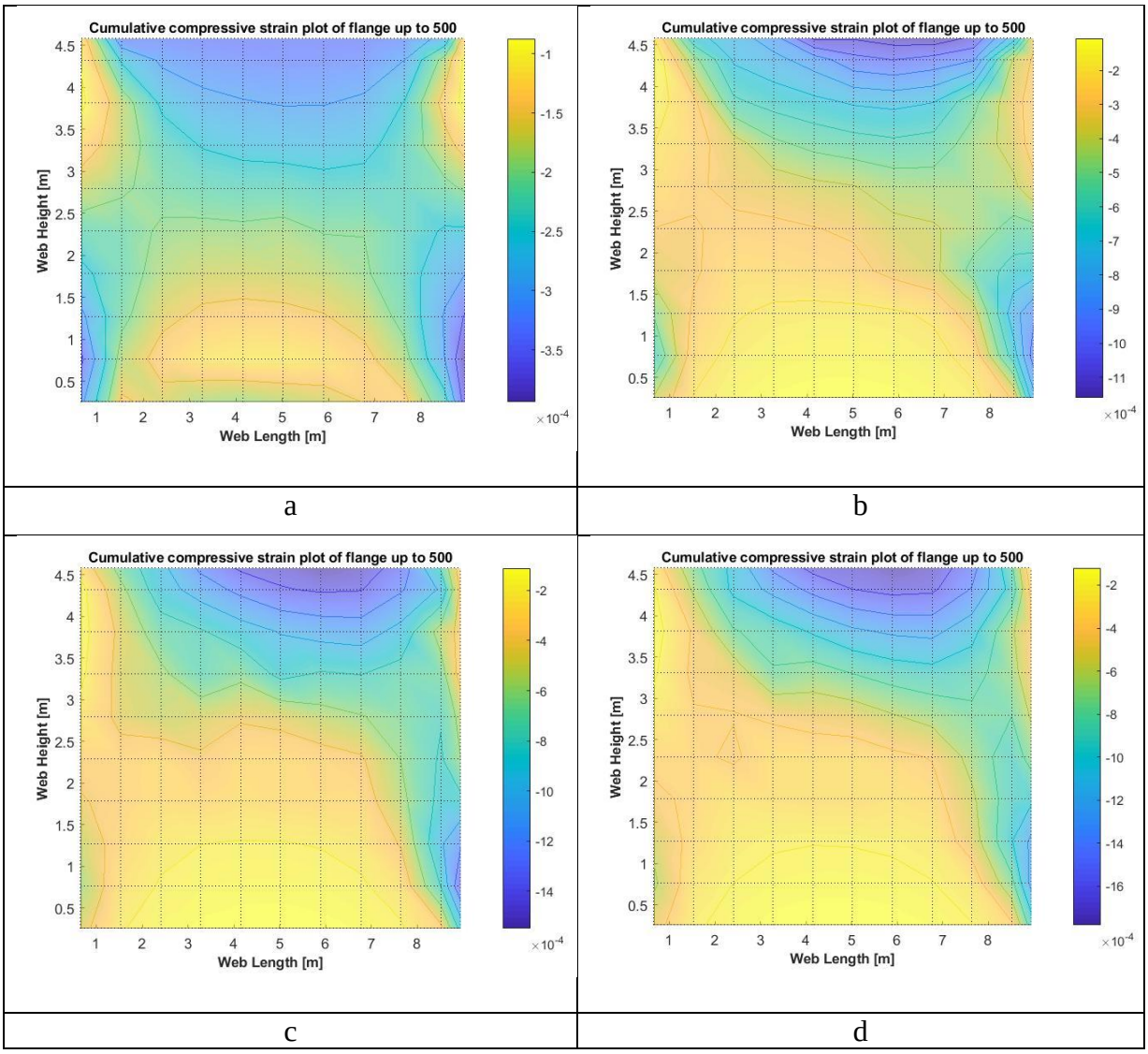

Figure 21. *Compressive contour plot of yz-panel in the four buildings. (a) is 4-story building contour plot, (b) is 8-story building contour plot, (c) is 12-story building contour plot, (d) is 16-story building contour plot.*

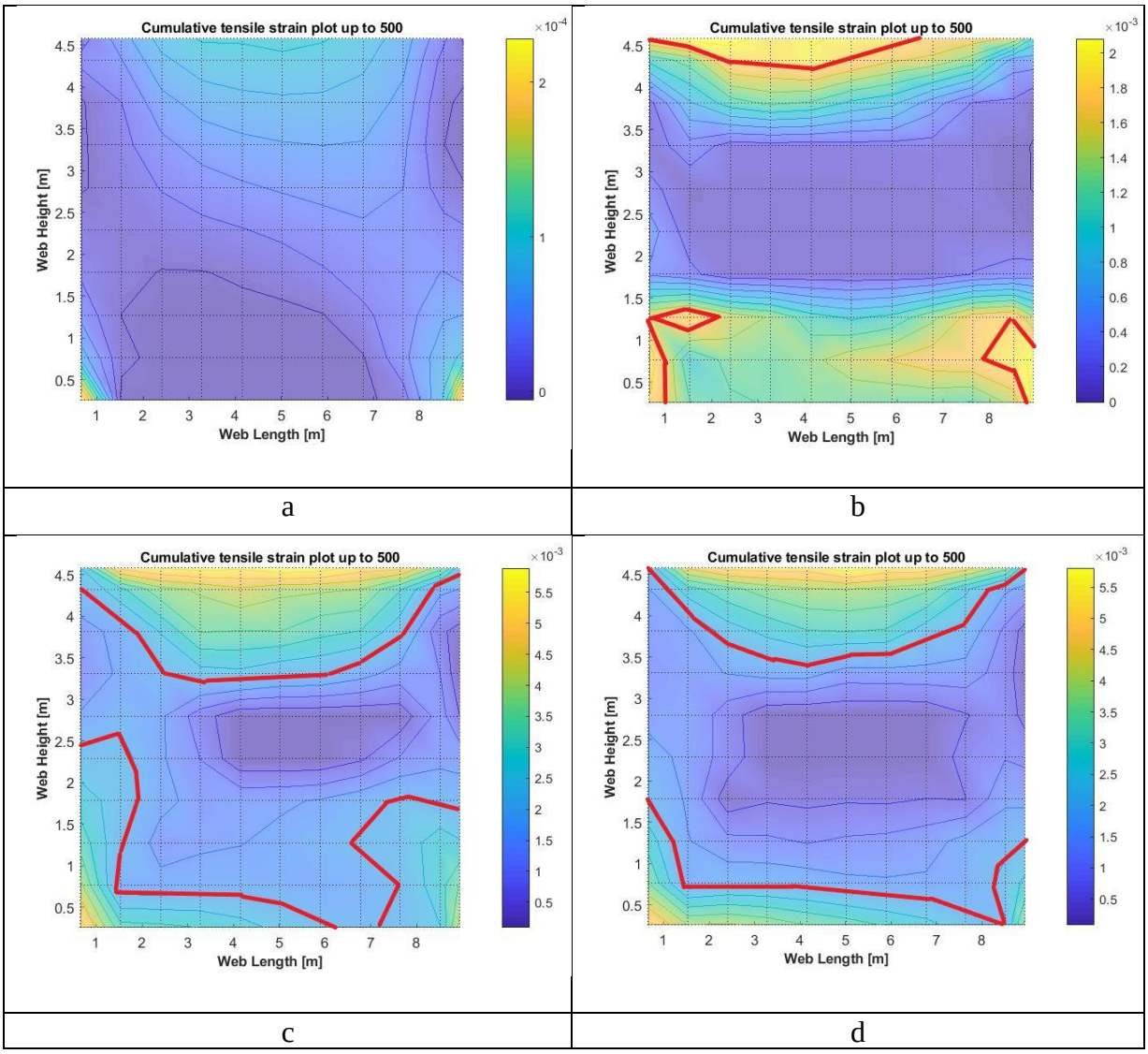

Figure 22. *Tensile contour plot of yz-panel in the four buildings. (a) is 4-story building contour plot, (b) is 8-story building contour plot, (c) is 12-story building contour plot, (d) is 16-story building contour plot*.

The yielding situation of xz-panel on the second floor in four buildings is shown in Figure 20. For 4-story building, the yielding showed in Figure 20(a) happened in the bottom right and left corners. In the 8-story building, the bottom corner yielding area develops to the entire length of bottom xz-panel which is shown in Figure 20(b). Meanwhile, the top of the wall also happened yielding in 8-story building, but the area is small. In Figure 20(c), the height of the bottom yielding area increases and the top yielding area developed to the entire length of the top of the panel. For 16-story building, in Figure 20(d), the top and the bottom yielding area are similar to the area in the 12-story building. The red line marked the yielding area. From Figure 21, we can see the yz-panel didn't undergo crushing in the second floor of the four target buildings.

In Figure 22(a), the yielding didn't happen in yz-panel of the 4-story building. In the 8-story building, the yielding happened in the top middle area and both bottom corners, the total area is very small shown in Figure 22(b). In Figure 22(c) and 22(d), we can see the yielding area grew from the top middle area and both bottom corners to the center of the panel. The yielding area of the 12-story building and the 16-story building is similar. The top middle area and bottom left area happened serious yielding.

From the figures above, the crushing yielding area is increasing with the total number of floors increases. The crushing and yielding usually start from bottom corners of the wall and middle top area, then develop to the center area of the wall. The figures shown above are verified by the stress vs. strain steel bar plots in Appendix C.

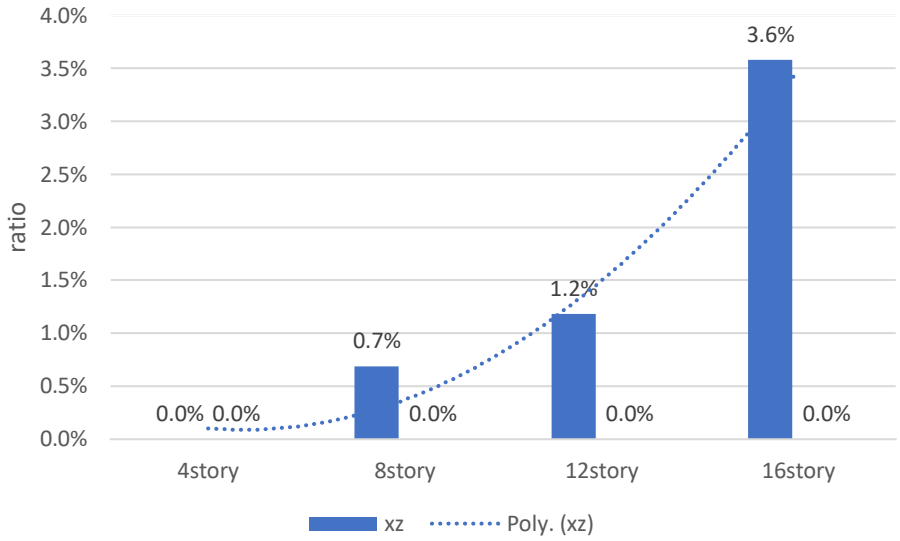

Figure 23. *Crushing area ratio for the second floor in the four buildings*

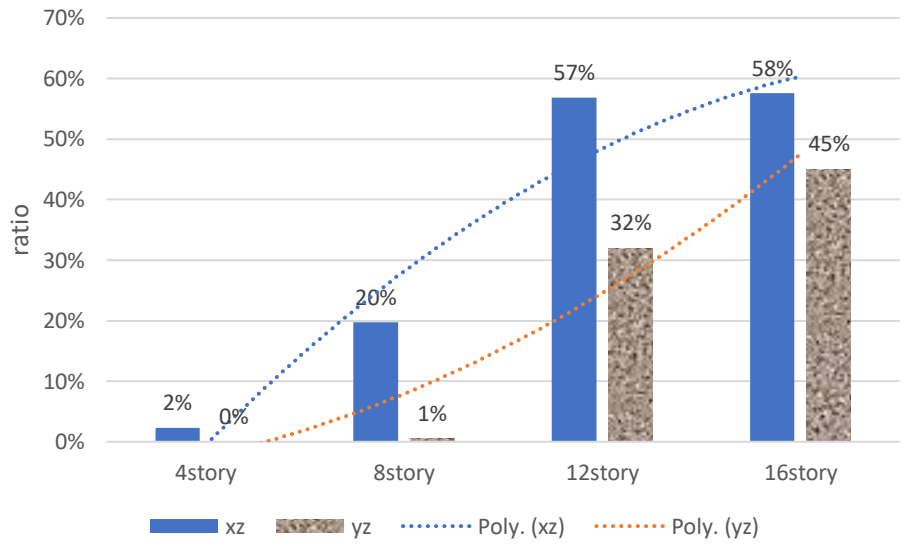

Figure 24. *Yielding area ratio for the second floor in the four buildings*

The crushing area ratio for the box-shaped wall in the second floor of four buildings is shown in Figure 23. Here, the area ratio of the crushed zone is defined by the area ratio of the crushed zone to the total area of the panel. From the figure, we can see the yz-panel didn't happen crushing. The crushing area ratio double increases with the height of the building increases in xz-panel. The growth trend exhibits a convex parabolic shape with vary height. Even if crushing happened, the crushing area ratio for 16-story building is 3.58% that is relatively small. The damage is not destructive.

The yielding area ratio situation for the box-shaped wall in the second floor of four building is shown in Figure 24. Based on the figure, we can see the yielding area increases with the height of the building grows. However, the growth pattern is different for two panels. The trend line of xz- panel with varying building heights exhibits a convex parabolic shape and the one of yz- panel is a concave parabolic shape. The xz-panel is aligned with y-directional ground acceleration, which is the mainly resisting the excitation. The yielding ratio for both directions panels of 12-story and the 16-story building is similar and the values are larger than the lower buildings. The building lower than the 12-story building is relatively safe and the building with twelve and more stories may happen fatal damage from the second floor, such as tilt down.

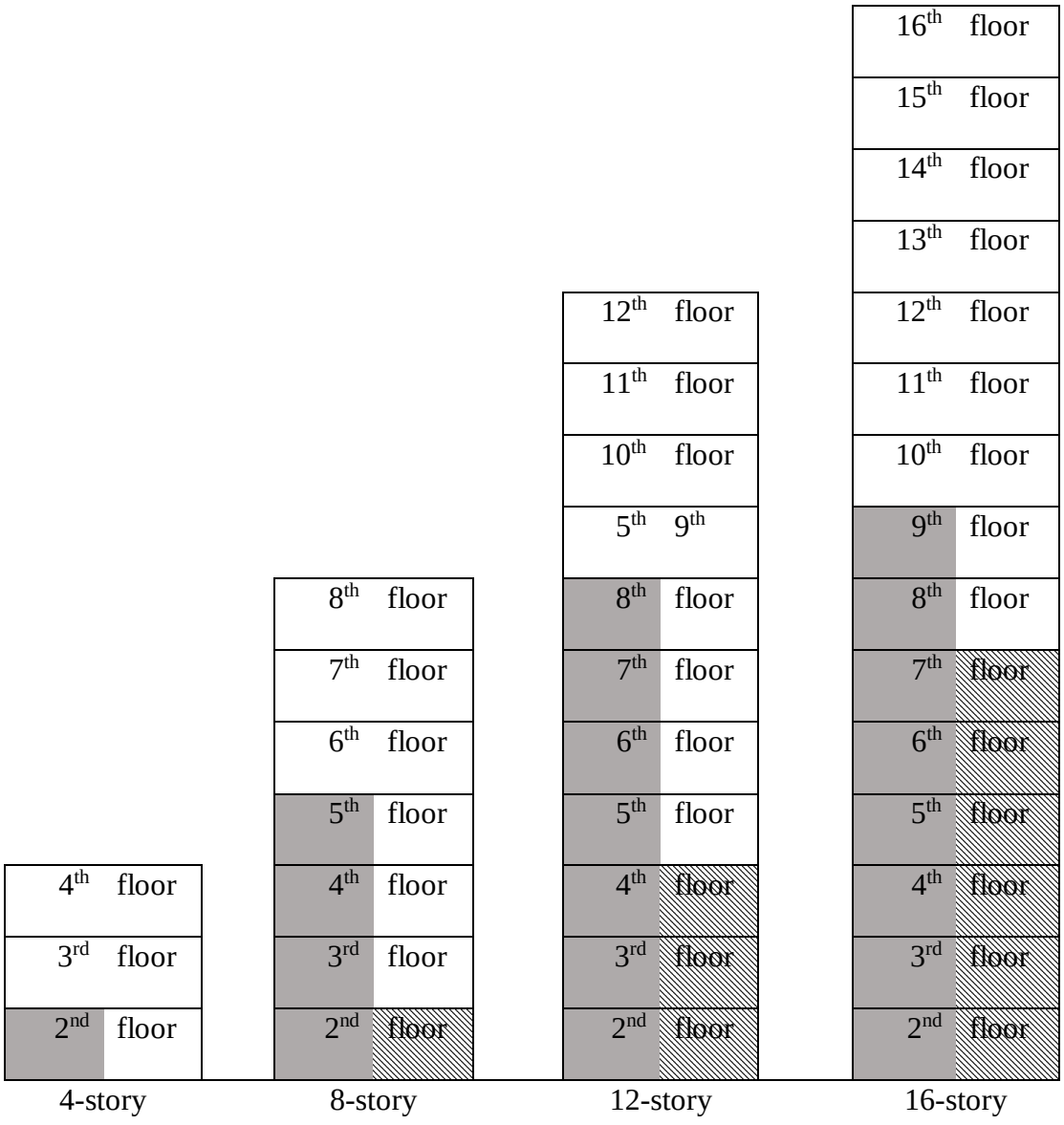

Figure 25. *The crushing and yielding situation of xz-panel of the box-shaped wall in the four buildings. The grey area means the floor happened yielding and the slashed area means the floor happened crushing.*

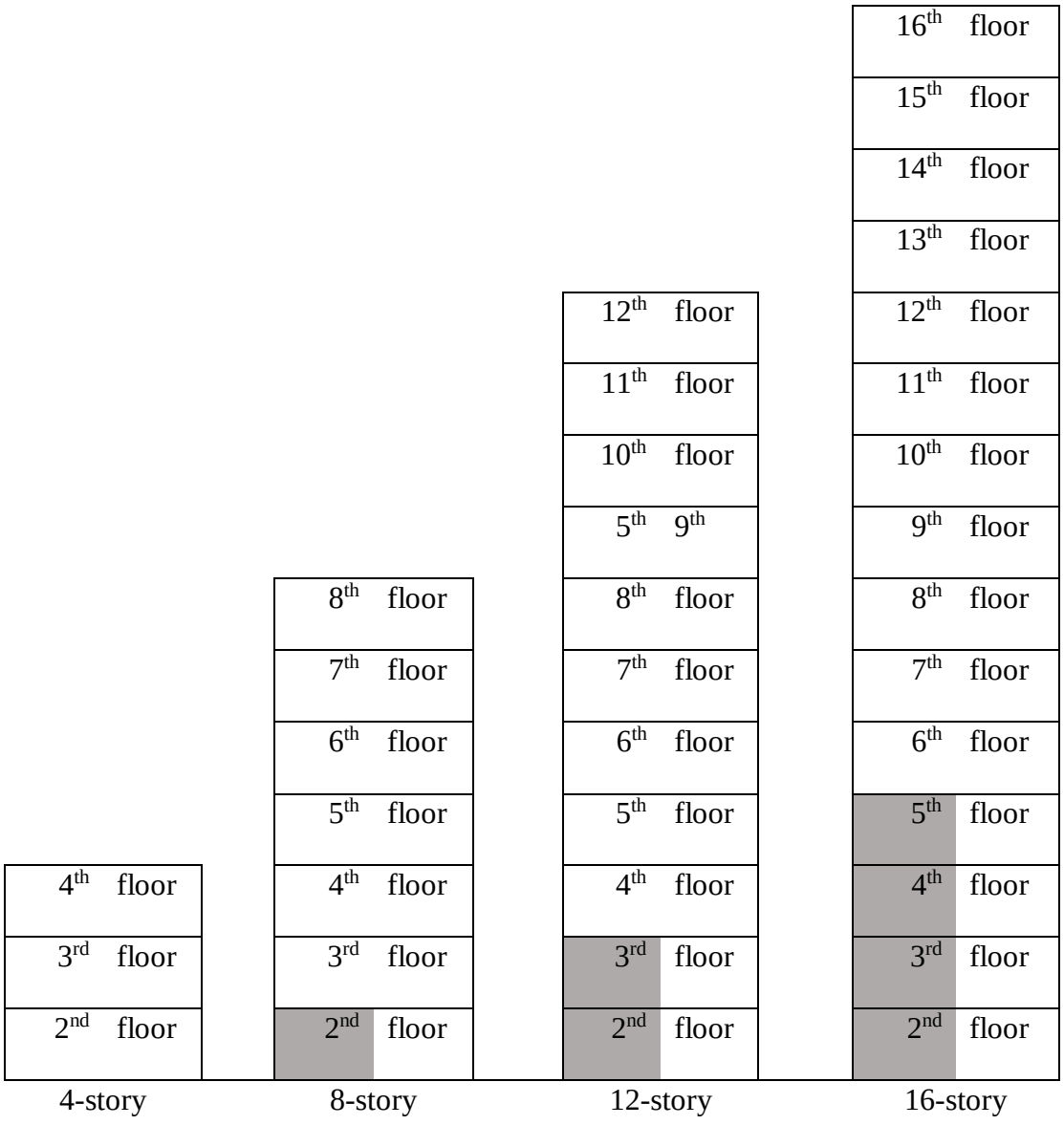

Figure 26. *The crushing and yielding situation of yz-panel of box-shaped wall in the four buildings. The grey area means the floor happened yielding and the slashed area means the floor happened crushing.*

The yielding and crushing not only happened on the second floor. For higher building, the other floors also have happened yielding and crushing. In Figure 25, the yielding and crushing situation of xz-panel is shown. The floor happened yielding is in grey, and the one happened crushing is in slash. With the building height increases, the number of floors happened yielding and crushing is increases. The yz-panel relative information is shown in Figure 26. The crushing didn't generate for all buildings. Even though the yielding area in yz-panel happened less than xz-panel, it still follows the rule that is the number of the floor with yielding increases with the height of building increases. The main resisting system is xz-panel. The crushing didn't happen in yz-panel and the number of floors happened yielding is less than xz-panel in the same building.

On the same floor, there are two L-shaped walls located on the other side of the box-shaped wall. Under the same ground excitation, the yielding and crushing happened in the L-shaped walls are different with the box-shaped wall.

In Figure 27, the ground floor of the 4-story building did not happen yielding, and the one of the 8-story building happened in the right bottom of the xz-panel. For the 12-story and 16-story building, the yielding happened three sides of the xz-panel that are top, right and bottom sides. With the height of the building increases, the yielding happened more seriously, and the area of the yielding is becoming larger.

In Figure 28, only the 12-story building and 16-story building happened crushing for xz- panel. In the 12-story, the crushing just happened in the right bottom corner. The crushing developed in the two bottom corners and left the top corner in the 16-story building and the area of crushing is larger than the one in the 12-story building.

The yielding developed in the xz- panel of the second floor of four buildings obviously. It did not happen in the 4-story building. In the 8-story building, the crushing area happens from the bottom. It grew from right bottom corner to the half-right wall in the 12-story building. For the 16-story building, the crushing grew to entire wall beside the smaller area the red line marked.

In the yz-panel on the second floor, the crushing just occurred in the 16-story building. The yielding area is in two bottom corners. All L-shaped wall contour plots are proved by the stress vs. strain steel bar plots in Appendix D.

The yielding didn't happen in the L-shaped walls in the second floor of the lower-rise building. No matter which direction of the wall, the high-rise building happened yielding in the bottom of the wall. For the crushing, it grows obvious with the height of building increases. It didn't happen in the 4-story building and happened from bottom corners in the 8-story building. As the height of the building increases to 12- and 16-story, the crushing area grows to half of wall or 3/4 of the entire wall.

In Figure 31, the yielding area ratio of the L-shaped wall of four buildings increases with building height. The tensile damage of the steel in yz-direction panel is more severe than xz-direction panel, which exhibits the yz panel is the primary resisting the excitation. The trend of the ratio is convex parabolic in both direction panels. In taller building (12- and 16-story), the yielding ratio appears to be severe and the value of the yielding ratio is higher than 50%. The building height may enhance the steel yielding on the second floor.

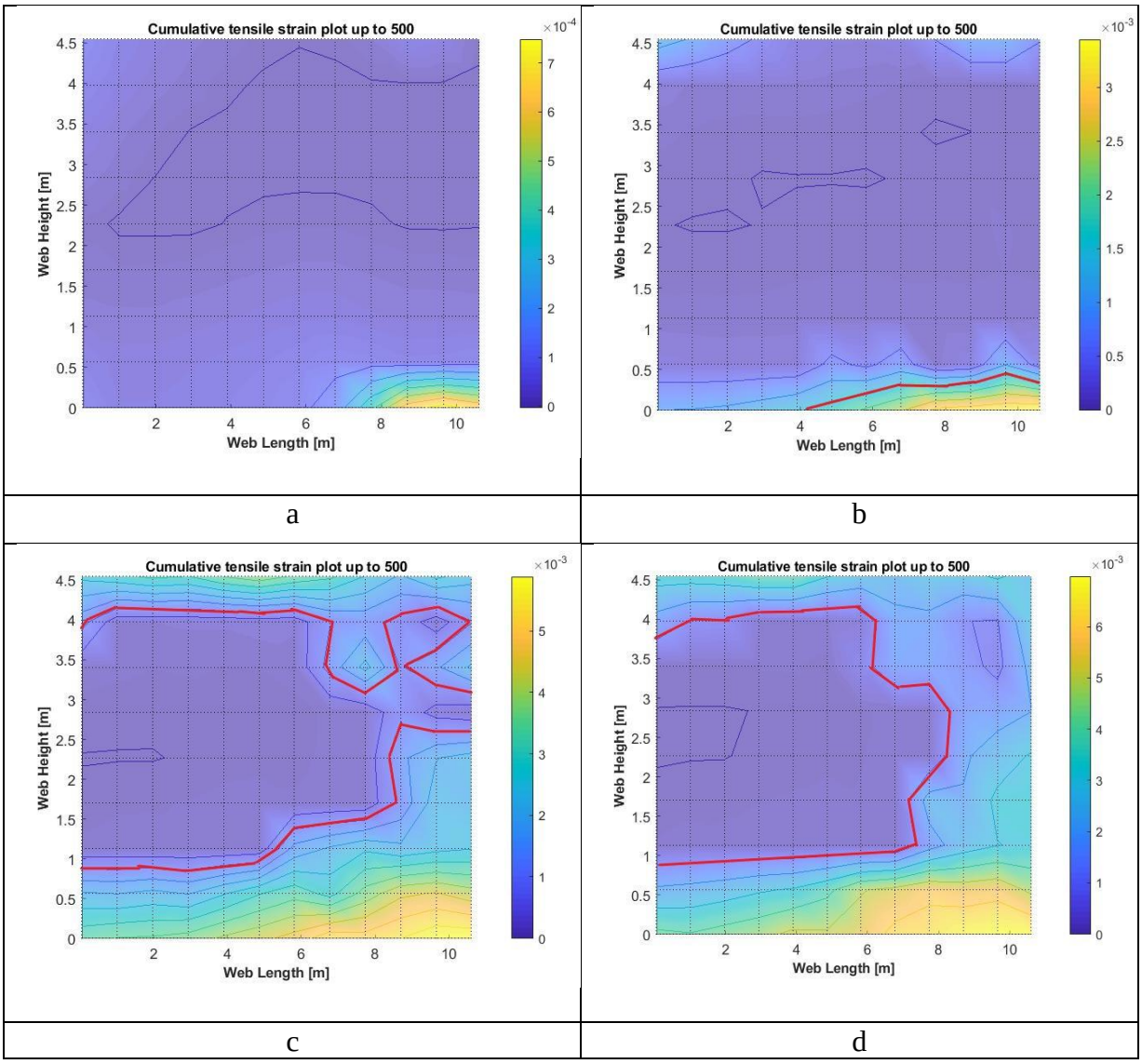

Figure 27. *Tensile contour plot of xz--panel in the four buildings. (a) is 4-story building contour plot, (b) is 8-story building contour plot, (c) is 12-story building contour plot, (d) is 16-story building contour plot.*

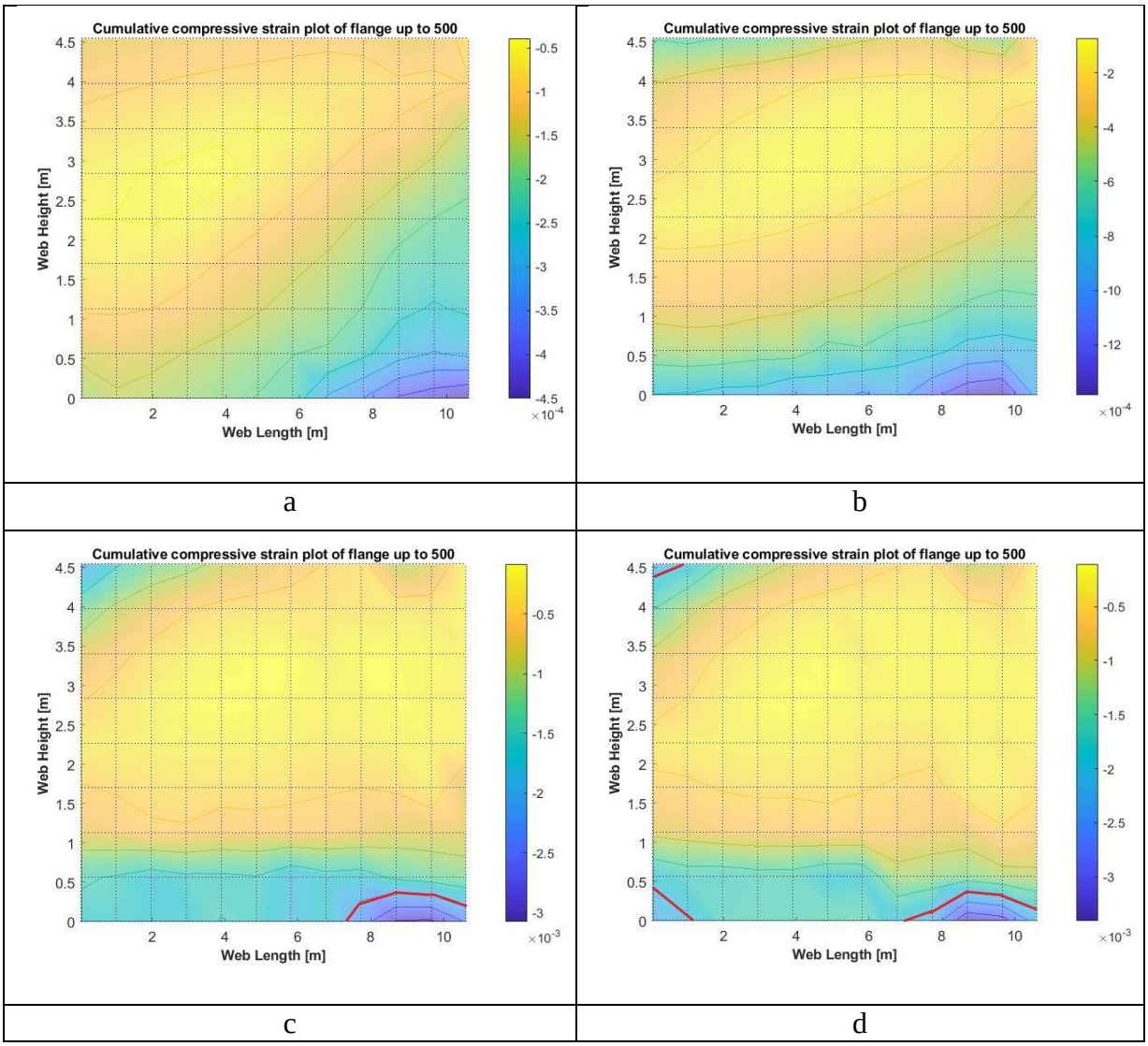

Figure 28. *Compressive contour plot of xz-panel in the four buildings. (a) is 4-story building contour plot, (b) is 8-story building contour plot, (c) is 12-story building contour plot, (d) is 16-story building contour plot.*

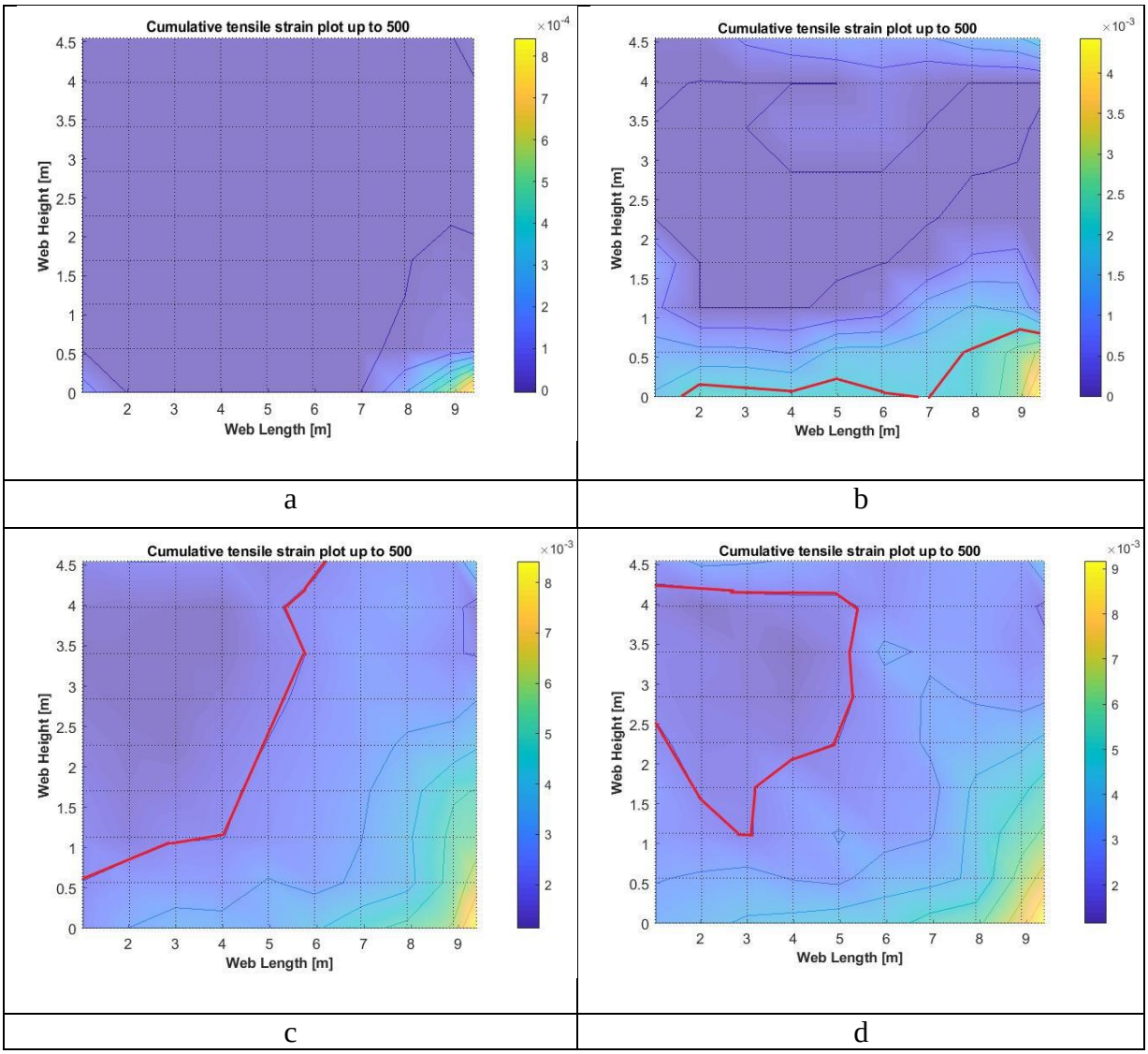

Figure 29. *Tensile contour plot of yz--panel in the four buildings. (a) is 4-story building contour plot, (b) is 8-story building contour plot, (c) is 12-story building contour plot, (d) is 16-story building contour plot.*

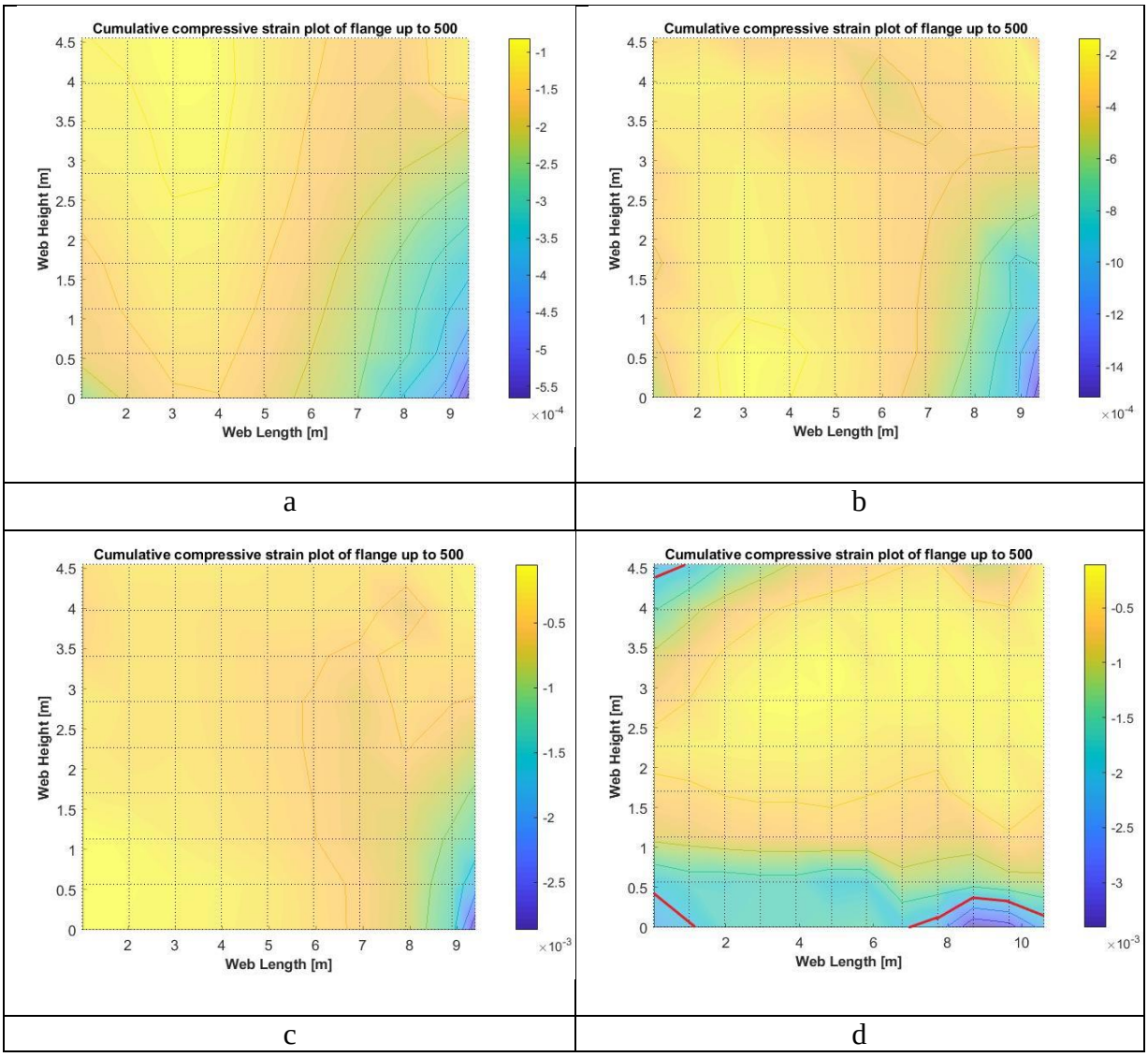

Figure 30. *Compressive contour plot of yz--panel in the four buildings. (a) is 4-story building contour plot, (b) is 8-story building contour plot, (c) is 12-story building contour plot, (d) is 16-story building contour plot.*

In detail, Figure 32 summarizes how crushing changes with varying building height. The yz-direction panel only occurs crushing damage in higher (16-story) building. Comparing with the yielding ratio, the value of the crushing is much smaller. In the xz panel, the crushing damage happened in the taller building (12- and 16-story), and the pattern of the crushed fraction is also convex parabolic shape.

3.3 Validations of General Application of VEEL

In this research, VEEL simulated the dynamic behavior of complex walls under the one-directional ground motion. Generally, VEEL only requires a few material properties while the entire geometry and complete reinforcement layout are automatically modeled by an in-house finite element preprocessing program. VEEL have proven cover a wide range of real-scale reinforced concrete structures without restriction to complex geometry and reinforcement layout. For the validations, other researchers' well-documented experimental results were thoroughly used. Barbell-shaped wall with opening rectangular [25] and T-shaped walls [26, 27], and an H-shaped wall [27] are all validated the result by VEEL. In Dr. Cho's paper, VEEL does the simulations demonstrate overall accuracy and general applicability [18]. Compared to many existing macroscopic wall models available in the literature (e.g., [26, 27]), VEEL can offer direct access to microscopic nonlinear damage phenomena, notably during building's dynamic motions. VEEL's ability to capture complex microscopic damage is promising: e.g., VEEL can realistically describe "progressive" bar buckling and associated concrete spalling. It is true that many existing macroscopic wall models in the literature (e.g., [27, 28] show good accuracy in global force-displacement prediction.

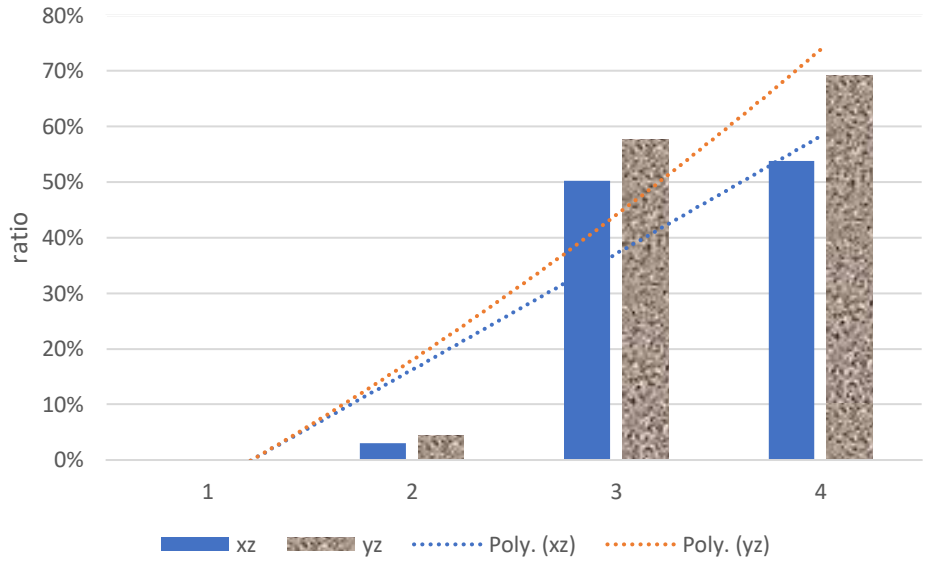

Figure 31. *Yielding area ratio for the second floor in the four buildings*

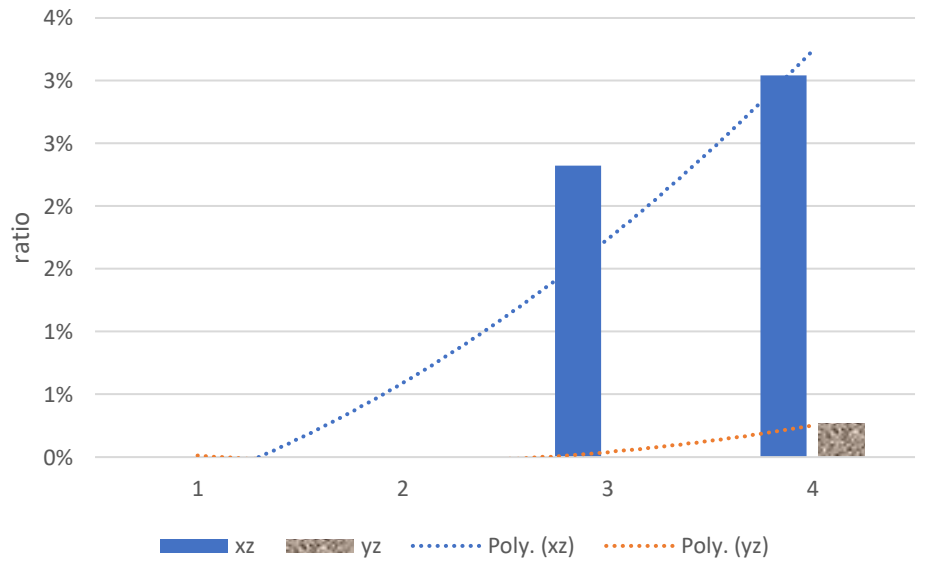

Figure 32. *Crushing area ratio for the second floor in the four buildings*

CHAPTER 4. CONCLUSIONS

This study performed a novel multiscale dynamic analysis of four pre-1980 RCSW buildings with varying heights to improve our understanding of the nonlinear dynamic behavior of RCSW buildings. Three-stage multiscale nonlinear dynamic analysis platform takes advantage of multiscale FEA and parallel computing to perform coupled nonlinear dynamic analysis linked with the millimeter length scale's physical damage mechanisms and predict the entire building-level damage. By making use of the improved nonlinear material models, it offers direct access to complex wall's damage evolutions and wall-, floor- and building-level dynamic responses.

From the multiscale responses, one-directional excitation may lead to bi-directional and torsional deformations of RCSW building. As multidirectional damages on the primary structural component (box-shaped wall), the major contribution role of the core wall may shift to other structural components (L-shaped wall). With the height of the building increases, this kind of role shift happens earlier. The role shift exacerbates the multidirectional dynamic motions of the building. Meanwhile, the novel multiscale analysis exhibits how one-direction ground excitation can result in localized damage in the primary walls in other direction. The damage in multiple levels is aggravated by increasing building height. Meanwhile, the vertical irregularity leads to damage concentration on the second soft floor.

CHAPTER 5. FUTURE WORK

From the result and analysis described above, the height of buildings can affect microscopic damage in varying degrees. In this case, the ground motion didn't cause serious damage. In the future, the impact of height on the microscopic damage can be investigated by extreme ground motion in multiple directions. Thus, future extensions shall include more microphysical mechanisms such as integrative consideration of bar slip, strain penetration, and progressive buckling with element-level geometric nonlinearity

To assure general applicability and accuracy, a future extension should be validated against shake table experiments. The result may be different from reality, the experimental research on complex RCSW system subject to multi-directional, irregular loading conditions is needed to validate the accuracy and general application.

With the popularity of Artificial Intelligence technology, the microscopic damage can be predicted by machine learning models, such as decision trees, super-vector machine. The contrast of the result predicted by machine learning and the one estimated by VEEL is an interesting topic.

REFERENCES

1. Concrete Coalition. The Concrete Coalition and the California Inventory Project: An Estimate of the Number of Pre-1980 Concrete Buildings in the State. EERI, CA, 2003

2. Massone LM, Bonelli P, Lagos R, Lüders C, Moehle J, Wallace JW. Seismic design and construction practices for RC structural wall buildings, Earthquake Spectra 2012; 28(S1): S245-S256.

3. Moehle J. February 27, 2010, Chile Earthquake Reconnaissance Team Investigation Report, Earthquake Engineering Research Institute (EERI) 2010.

4. Okazaki T, Lignos DG, Midorikawa M, Ricles JM, Love J. Damage to steel buildings observed after the 2011 Tohoku-Oki earthquake, Earthquake Spectra 2013; 29(S1): S219-S243.

5. Okawa I, Kashima T, Koyama S, Iiba M. Recorded responses of building structures during the 2011 Tohoku-Oki earthquake with some implications for design practice. Earthquake Spectra 2013; 29(S1): S245-S264.

6. Reynouard JM, Fardis MN eds. Shear wall structures. Cafeel-Ecoest Thematic Report No.5. R. T. Severn and R. Bairrao (LNEC, ISBN 972-49-1891-2), Sep 2001; 240.

7. SMART 2013, Seismic design and best-estimate Methods Assessment for Reinforced concrete buildings subjected to Torsion and non-linear effects, CEA, Oxand, France.

8. Kabeyasawa T, Kato S, Sato M, Fukuyama H, Kabeyasawa T, Tani M, Kim Y, Hosokawa Y.Effects of bi-directional lateral loading on the strength and deformability of reinforced concrete walls with/without boundary columns. Proc. of the 10th NCEE, EERI, 2014.

9. Pégon P, Plumier C, Pinto A, Molina J, Gonzalez P, Tognoli PC, Hubert O. U-shaped walls: Description of the experimental set-up. TMR-ICONS-TOPIC5, JRC Ispra, Italy, 2000; 23.

10. Cho I, Porter KA. Three-Stage Multiscale Nonlinear Dynamic Analysis Platform for Tackling Building Classes. Earthquake Spectra 2014.

11. Mulas MG, Coronelli D, Martinelli L. Multi-scale modeling approach for the pushover analysis of existing RC shear walls-Part I: Model formulation. Earthquake Eng Struc 2007; 6:1169-1187.

12. Mazzoni S, McKenna F, Scott M, Fenves G. Opensees command language manual, Pacific Earthquake Engineering Research (PEER) Center 2005.

13. Cho I. Multilayered grouping parallel algorithm for multiple-level multiscale analyses. International Journal for Numerical Methods in Engineering 2014; 100, 914-932.

14. Thomsen JH, IV, Wallace JW. Displacement-based design of reinforced concrete structural walls: Experimental studies of walls with rectangular and T-shaped cross-sections. Technical Report CU/CEE-95/06, Department of Civil and Environmental Engineering, Clarkson University: Potsdam, N. Y., 1995.

15. Cho I. Virtual earthquake engineering laboratory for capturing nonlinear shear, localized damage, and progressive buckling of the bar. Earthquake Spectra 2013; 29(1):103–126.

16. Thorenfeldt, E., Tomaszewicz, A., and Jensen, J. J. (1987). Mechanical properties of high-strength concrete and applications in design. Proc., Symp. Utilization of High-Strength Concrete, American Concrete Institute (ACI), Farmington Hills, MI.

17. Feenstra, P. H., Rots, J. G., Arnesen, A., Teigen, J. G., and Høiseth, K. V.(1998). Computational modeling of concrete structures, R. de Borst et al., eds., Balkema, Rotterdam, Netherlands, 13–22.

18. Cho, I., and Hall, J. F. (2012). "Parallelized implicit nonlinear FEA program for real scale RC structures under cyclic loading." J. Comput. Civ. Eng., 10.1061/(ASCE)CP.1943-5487.0000138, 356–365.

19. Cho I, Porter K. Three-stage multiscale nonlinear dynamic analysis platform for building-level loss estimation. Earthquake Spectra 2015; 31 (2), 1021-1042.

20. Chopra, A. K., 2001. Dynamics of Structures, Prentice-Hall, Inc., Upper Saddle River, NJ, USA.

21. Krishnan, S., and Hall, J. F., 2006. Modeling steel frame buildings in three dimensions. I: Panel zone and plastic hinge elements, Journal of Engineering Mechanics 132, 345–358.

22. Rahul, and De, S., 2010. An efficient coarse-grained parallel algorithm for global-local multiscale computations on massively parallel systems, International Journal for Numerical Methods in Engineering 82, 379–402.

23. PEER Ground Motion Database. Pacific Earthquake Engineering Research (PEER) Center: Berkeley, CA, 2011: http://peer.berkeley.edu/peer_ground_motion_database/site.

24. Kabeyasawa T, Kato S, Sato M, Fukuyama H, Kabeyasawa T, Tani M, Kim Y, Hosokawa Y. Effects of bi-directional lateral loading on the strength and deformability of reinforced concrete walls with/without boundary columns. Proc. of the 10th NCEE, EERI, 2014.

25. Taylor CP, Cote PA, Wallace JW. Design of slender reinforced concrete walls with openings. ACI Structural Journal 1998; 95(4):420-433.

26. Thomsen IV JH, Wallace JW. Displacement-Based Design of Slender Reinforced Concrete Structural Walls-Experimental Verification. J Struct Eng-ASCE 2004; 130(4):618-630.

27. Orakal K, Wallace JW. Flexural Modeling of Reinforced Concrete Shear Walls - Experimental Verification. ACI Structural Journal 2006; 103(2):196–206.

28. Vecchio FJ. Towards Cyclic Load Modeling of Reinforced Concrete. ACI Structural Journal 40 1999; 96(2):193-202.

29. In Ho Cho and John F. Hall, 2014. General Confinement Model based on Nonlocal Information, ASCE Journal of Engineering Mechanics 140(6).

30. In Ho Cho, 2018, Deformation Gradient-Based Remedy for Mesh Objective Three-Dimensional Interlocking Mechanism, ASCE Journal of Engineering Mechanics, Vol. 144(1).

APPENDIX A. A SHORT VERSION OF INPUT FILE

%----------------------

% VEEL_MD 4-story 1970 building

% core #8 (the same as #5 and #7) on 1st floor

% originally loaded in the X direction

%

% Jan 05, 2015

%----------------------

INPUT INFORMATION

node	34268
element	27036
surface_force	0
nodal_force	959
nodal_reference_force	1918
specified_displacement	0
fixed_boundary	959
material	9
hysteresis	9
integration	2
output	0
displacement_history_data	2
perfectly_bonded_steel	13490

END INPUT INFORMATION

COORDINATE

1	3.04800000e+00	0.00000000e+00	0.00000000e+00
2	3.10000000e+00	0.00000000e+00	0.00000000e+00
3	3.58522222e+00	0.00000000e+00	0.00000000e+00

.	.	.	.
.	.	.	.
.	.	.	.
34262	7.51800000e+00	8.87776923e+00	4.98240000e+00
34263	6.90800000e+00	8.94900000e+00	4.98240000e+00
34264	6.95900000e+00	8.94900000e+00	4.98240000e+00
34265	6.98177778e+00	8.94900000e+00	4.98240000e+00
34266	6.99725000e+00	8.94900000e+00	4.98240000e+00
34267	7.46700000e+00	8.94900000e+00	4.98240000e+00
34268	7.51800000e+00	8.94900000e+00	4.98240000e+00

BOUNDARY CONDITION

1	1	1	1
2	1	1	1
3	1	1	1
.	.	.	.
.	.	.	.
.	.	.	.
957	1	1	1
958	1	1	1
959	1	1	1

NODAL FORCE

33310	0.00E+00	0.00E+00	-1879.19
33311	0.00E+00	0.00E+00	-1879.19
33312	0.00E+00	0.00E+00	-1879.19
.	.	.	.
.	.	.	.
.	.	.	.

34266 0.00E+00 0.00E+00 -1879.19

34267 0.00E+00 0.00E+00 -1879.19

34268 0.00E+00 0.00E+00 -1879.19

NODAL REFERENCE FORCE

33310 1.00E+00 0.00E+00 0.00E+00

33311 1.00E+00 0.00E+00 0.00E+00

33312 1.00E+00 0.00E+00 0.00E+00

. . . .

. . . .

. . . .

34266 0.00E+00 2.00E+00 0.00E+00

34267 0.00E+00 2.00E+00 0.00E+00

34268 0.00E+00 2.00E+00 0.00E+00

ELEMENT FORCE

MATERIAL

1	2.75150E+10	0.15	2402.0	0.23	1	//concrete
2	20E+10	0.3	0.0	0.3	2	//steel_No_4, ASTM A615 GR40
3	20E+10	0.3	0.0	0.3	3	//steel_No_11, ASTM A615 GR60
4	20E+10	0.3	0.0	0.3	4	//steel_No_14, ASTM A615 GR60
5	20E+10	0.3	0.0	0.3	5	//steel_No_18, ASTM A615 GR60
6	20E+10	0.3	0.0	0.3	6	//steel_No_6, ASTM A615 GR60
7	2.75150E+14	0.15	0.0	0.23	7	//Elastic Stiff concrete
8	20E+10	0.3	0.0	0.3	8	//steel_No_5, ASTM A615 GR60
9	20E+10	0.3	0.0	0.3	9	//steel_No_8, ASTM A615 GR60

HYSTERESIS

1	14	-32.44E+6	-0.002	3.244E+6	1.26e-4	1.E-3	0.31

2	21	129e-6	280E+6	0.0014	0.008	500E+6	-0.02	0.2
3	10002	1006E-6	420E+6	0.0021	0.015	620E+6	-0.02	0.2
4	10002	1452E-6	420E+6	0.0021	0.015	620E+6	-0.02	0.2
5	10002	2581E-6	420E+6	0.0021	0.015	620E+6	-0.02	0.2
6	10002	284E-6	420E+6	0.0021	0.015	620E+6	-0.02	0.2
7	10	0						
8	10002	200e-6	420E+6	0.0021	0.015	620E+6	-0.02	0.2
9	21	509e-6	420E+6	0.0021	0.015	620E+6	-0.02	0.2

CONNECTIVITY

1	1	1	2	26	25	825	826	850	849
2	1	2	3	27	26	826	827	851	850
3	1	3	4	28	27	827	828	852	851
.	.	.	.	.	.	.	.	.	.
.	.	.	.	.	.	.	.	.	.
.	.	.	.	.	.	.	.	.	.
27034	7	33306	33307	32809	32808	34265	34266	33768	33767
27035	7	33307	33308	32810	32809	34266	34267	33769	33768
27036	7	33308	33309	32811	32810	34267	34268	33770	33769

PERFECTLY BONDED STEEL

1	8	26	850
2	8	27	851
3	8	31	855
.	.	.	.
.	.	.	.
.	.	.	.
13488	8	30963	30964
13489	8	32833	32834
13490	8	32881	32882

DISPLACEMENT HISTORY

34268 1

1 0.0000e+00

2 0.0121

DISPLACEMENT HIST.(SECONDARY)

34268 2

1 0.0000e+00

2 0.0121

NONLINEAR CONTROL DATA

2 15 3 0

NEWTON RAPHSON TOLERANCE

1.0000e-03 3.0000e-02

END INPUT FILE

APPENDIX B. THE SAMPLE RESULT OF POST-PROCESS ANALYSIS

Setting 1. Nodal reference force vs. Nodal displacement

displacement	force
0.0000020243	0
-0.000000077249	-38372
-0.00000037027	-38680
-0.00000085349	-39213
.	.
.	.
.	.

Setting 2. Steel stress vs. strain

strain	stress
-2.7287e-06	-5.4574e+05
-2.8378e-06	5.6756e+05
-5.2884e-06	-1.0577e+06
.	.
.	.
.	.

Setting 3: At a specific time, capture steel related information

node i	node j	strain	stress	L_buckling	index
26	850	0.0000e+00	0.0000e+00	2.5422e-01	1
850	1674	-6.6337e-06	-1.3267e+06	2.5422e-01	1
855	1679	-5.7786e-06	-1.1557e+06	2.5422e-01	1
.	.	.	.	.	.
.	.	.	.	.	.
.	.	.	.	.	.

APPENDIX C. THE STRESS VS. STRAIN PLOTS OF THE BAR FOR THE BOX-SHAPED WALLIN THE FOUR BUILDINGS

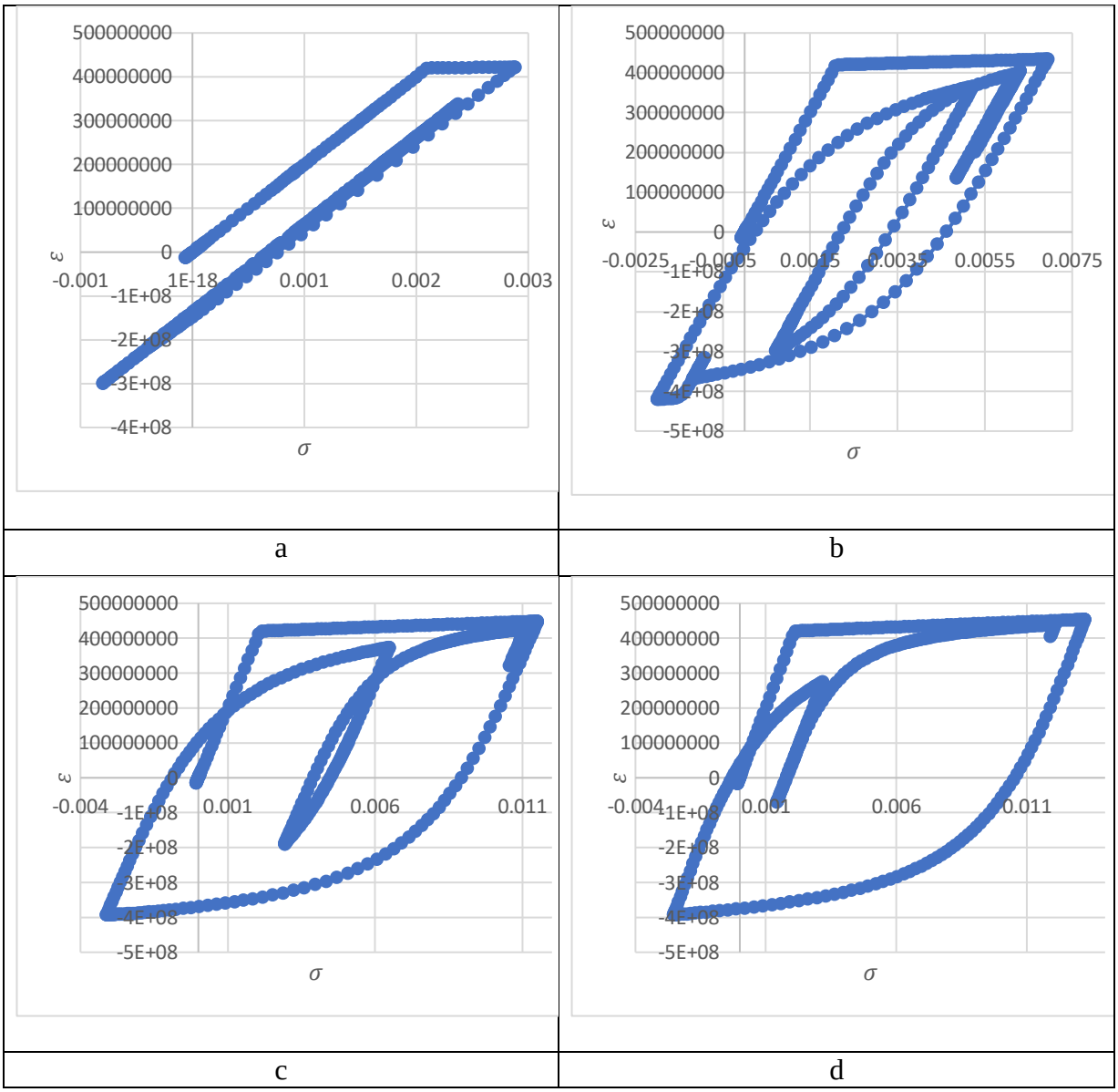

Figure 33. *Stress vs. strain plot of the bar in the right bottom corner xz—panel in the second floor in the four buildings. (a) is 4-story building stress vs. strain plot, (b) is 8-story building stress vs. strain plot, (c) is 12-story building stress vs. strain plot, (d) is 16-story building stress vs. strain plot.*

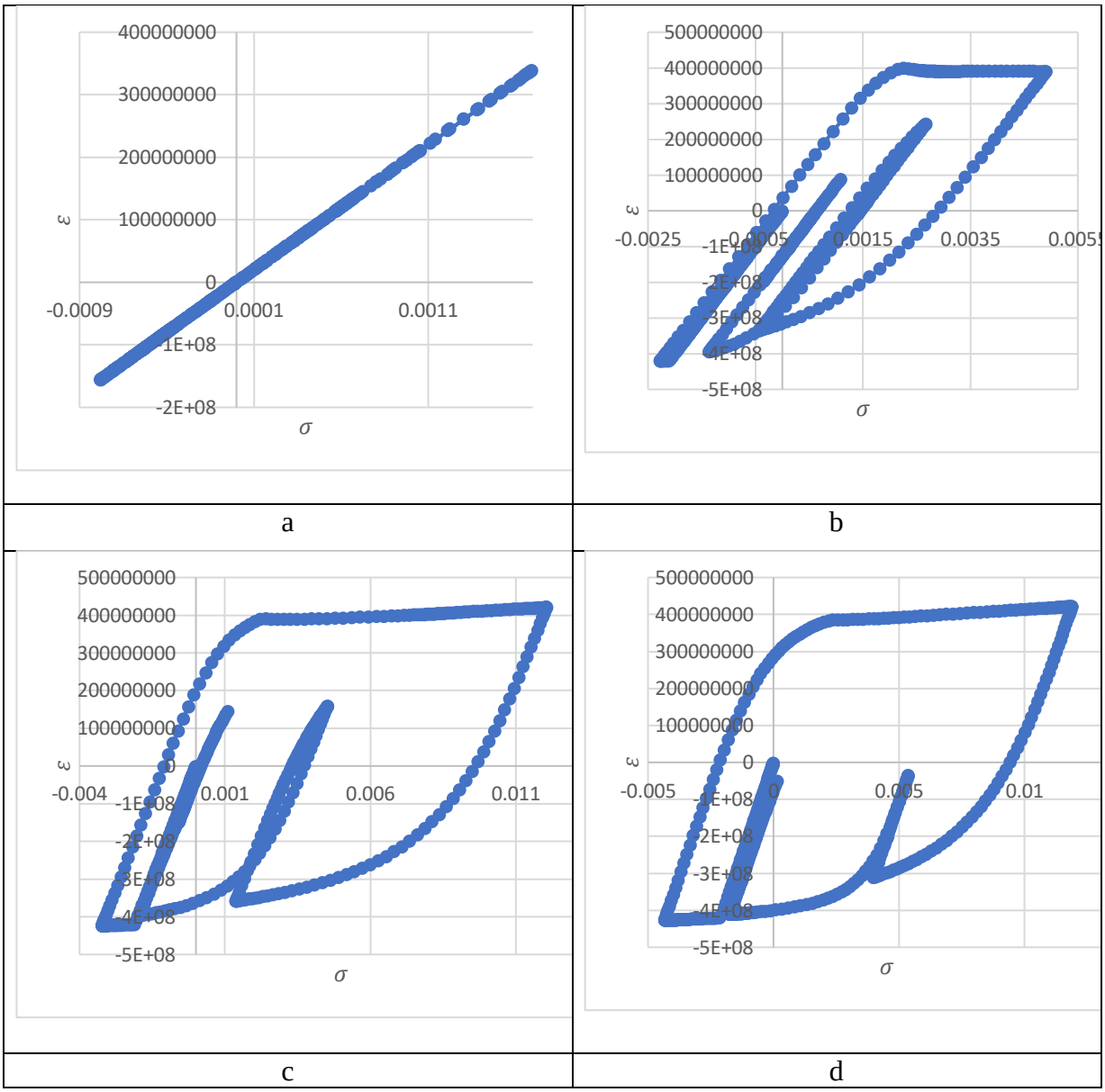

Figure 34. *Stress vs. strain plot of the bar in the left bottom corner xz--panel in the second floor in the four buildings. (a) is 4-story building stress vs. strain plot, (b) is 8-story building stress vs. strain plot, (c) is 12-story building stress vs. strain plot, (d) is 16-story building stress vs. strain plot.*

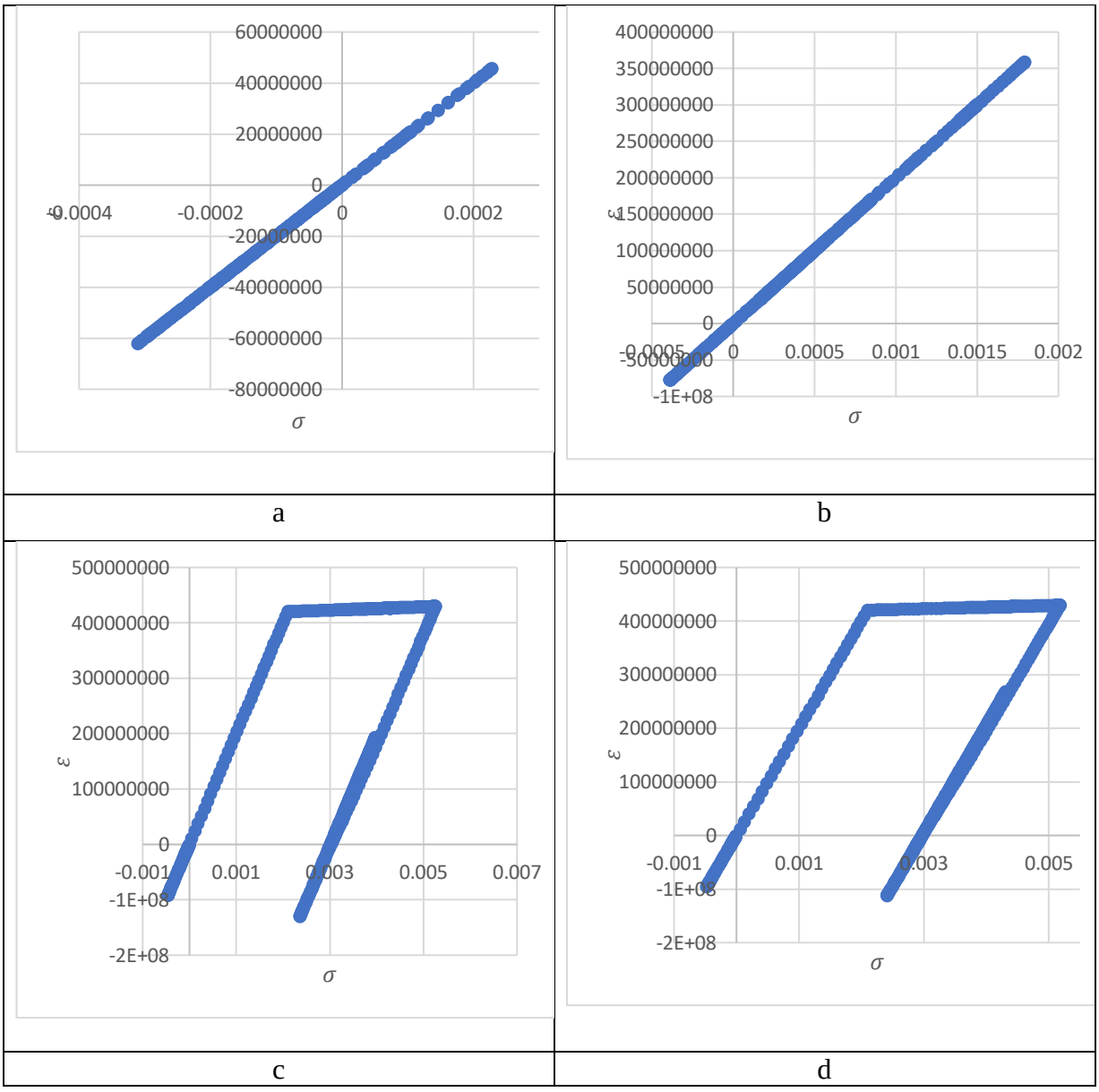

Figure 35. *Stress vs. strain plot of the bar in the right bottom corner yz--panel in the second floor in the four buildings. (a) is 4-story building stress vs. strain plot, (b) is 8-story building stress vs. strain plot, (c) is 12-story building stress vs. strain plot, (d) is 16-story building stress vs. strain plot.*

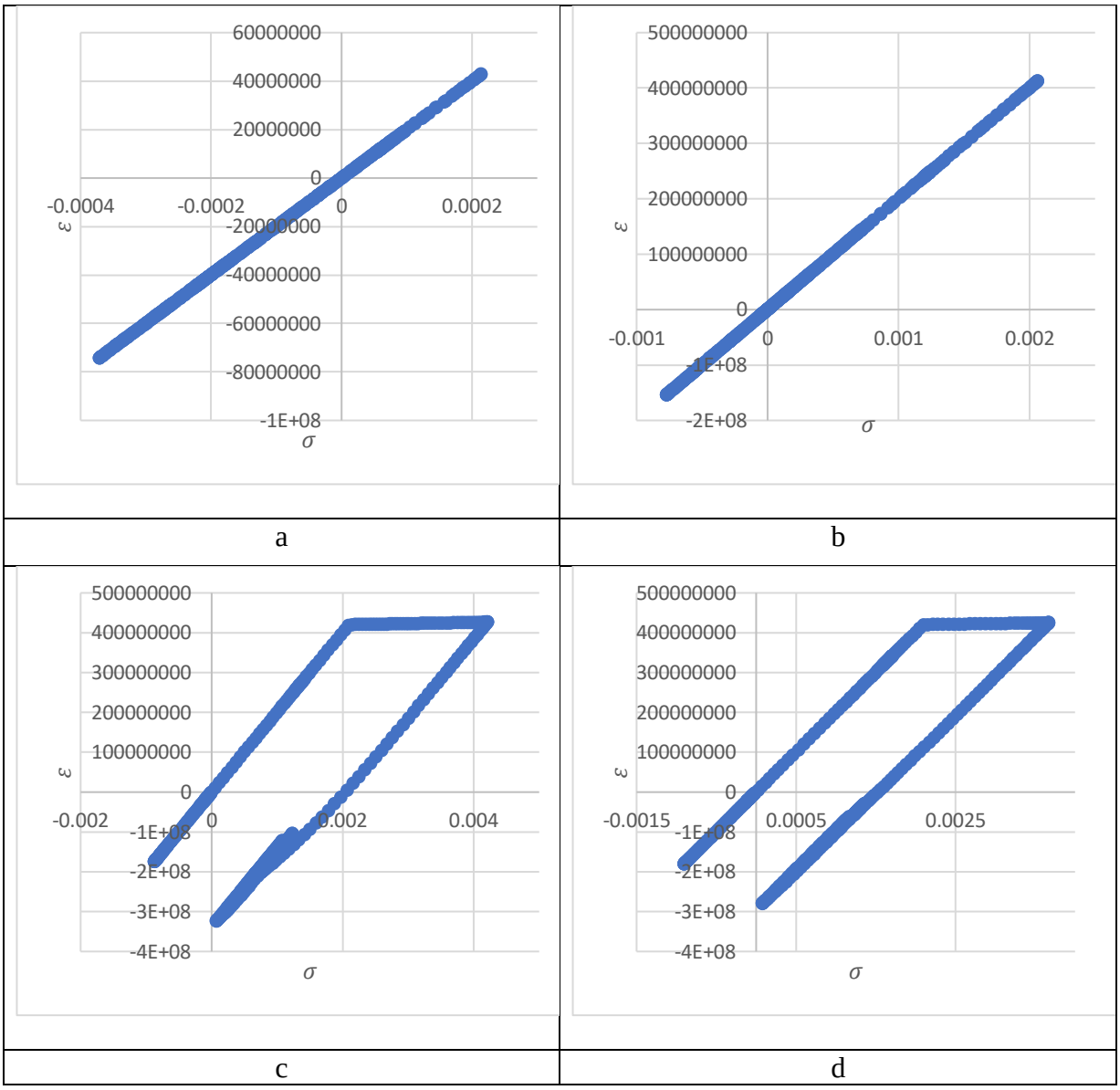

Figure 36. *Stress vs. strain plot of the bar in the left bottom corner yz--panel in the second floor in the four buildings. (a) is 4-story building stress vs. strain plot, (b) is 8-story building stress vs. strain plot, (c) is 12-story building stress vs. strain plot, (d) is 16-story building stress vs. strain plot.*

APPENDIX D. THE STRESS VS. STRAIN PLOTS OF THE BAR FOR THE L-SHAPED WALL IN THE FOUR BUILDINGS

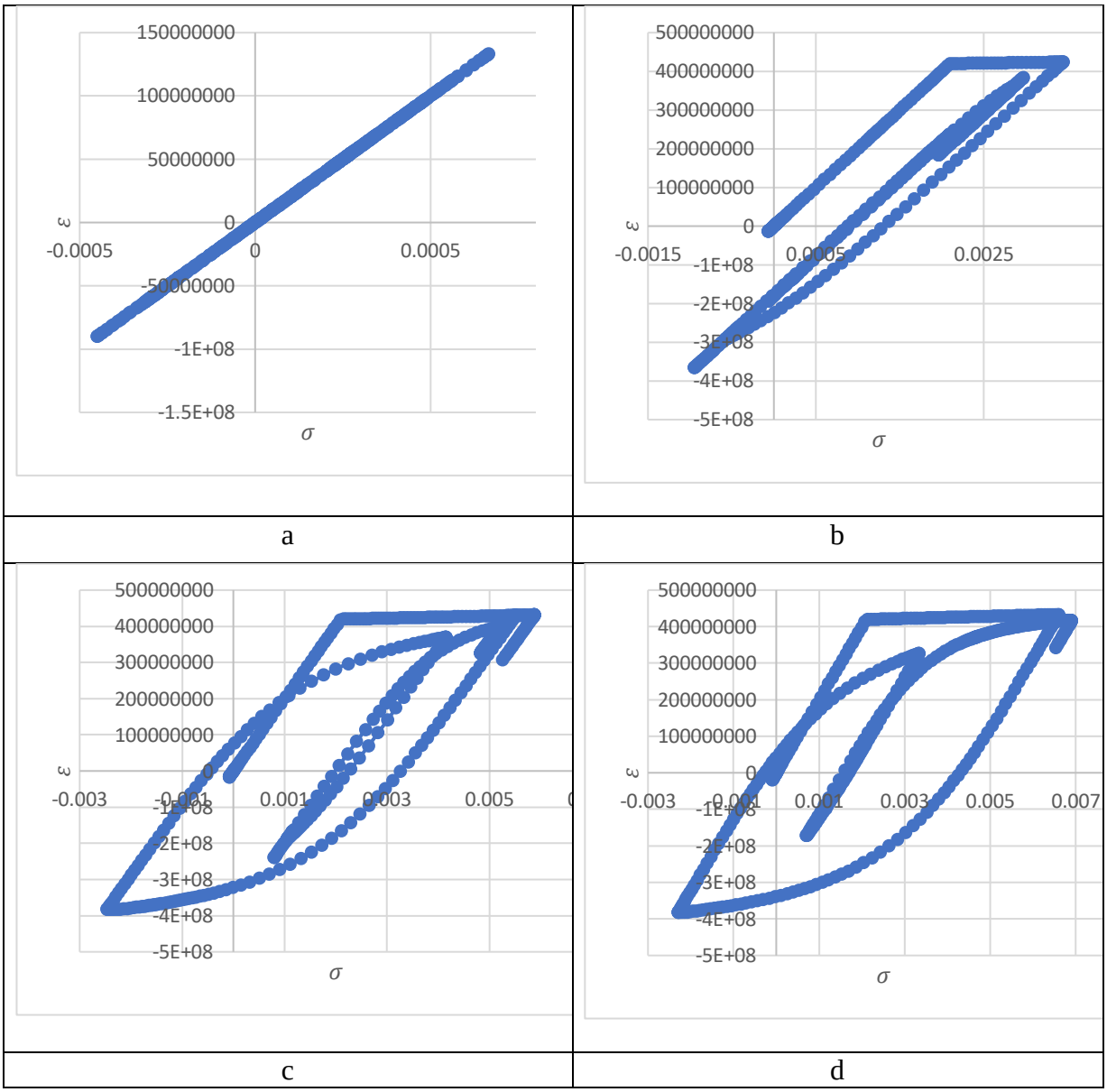

Figure 37. *Stress vs. strain plot of the bar in the right bottom corner xz—panel in the second floor in the four buildings. (a) is 4-story building stress vs. strain plot, (b) is 8-story building stress vs. strain plot, (c) is 12-story building stress vs. strain plot, (d) is 16-story building stress vs. strain plot.*

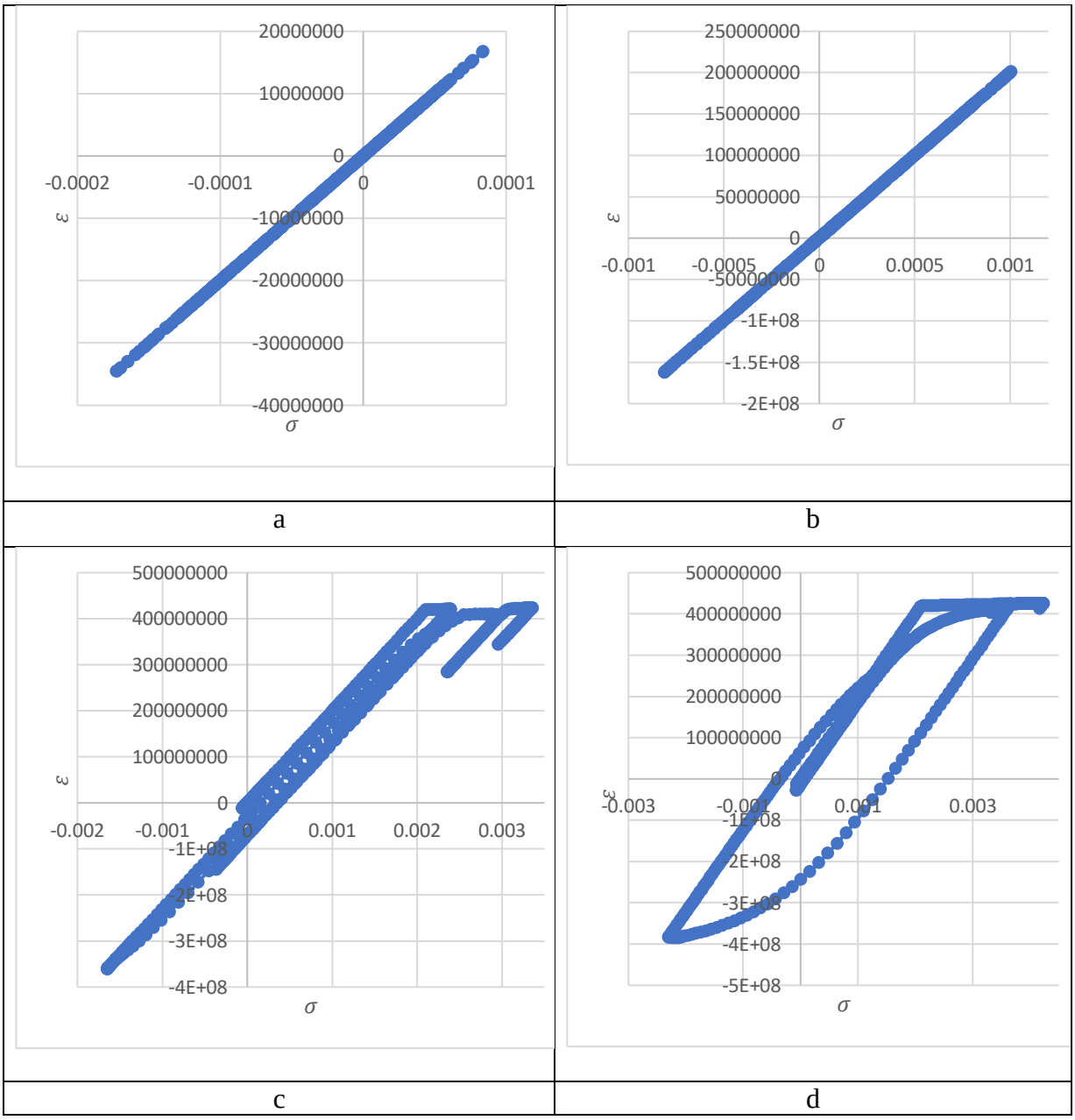

Figure 38. *Stress vs. strain plot of the bar in the left bottom corner xz--panel in the second floor in the four buildings. (a) is 4-story building stress vs. strain plot, (b) is 8-story building stress vs. strain plot, (c) is 12-story building stress vs. strain plot, (d) is 16-story building stress vs. strain plot.*

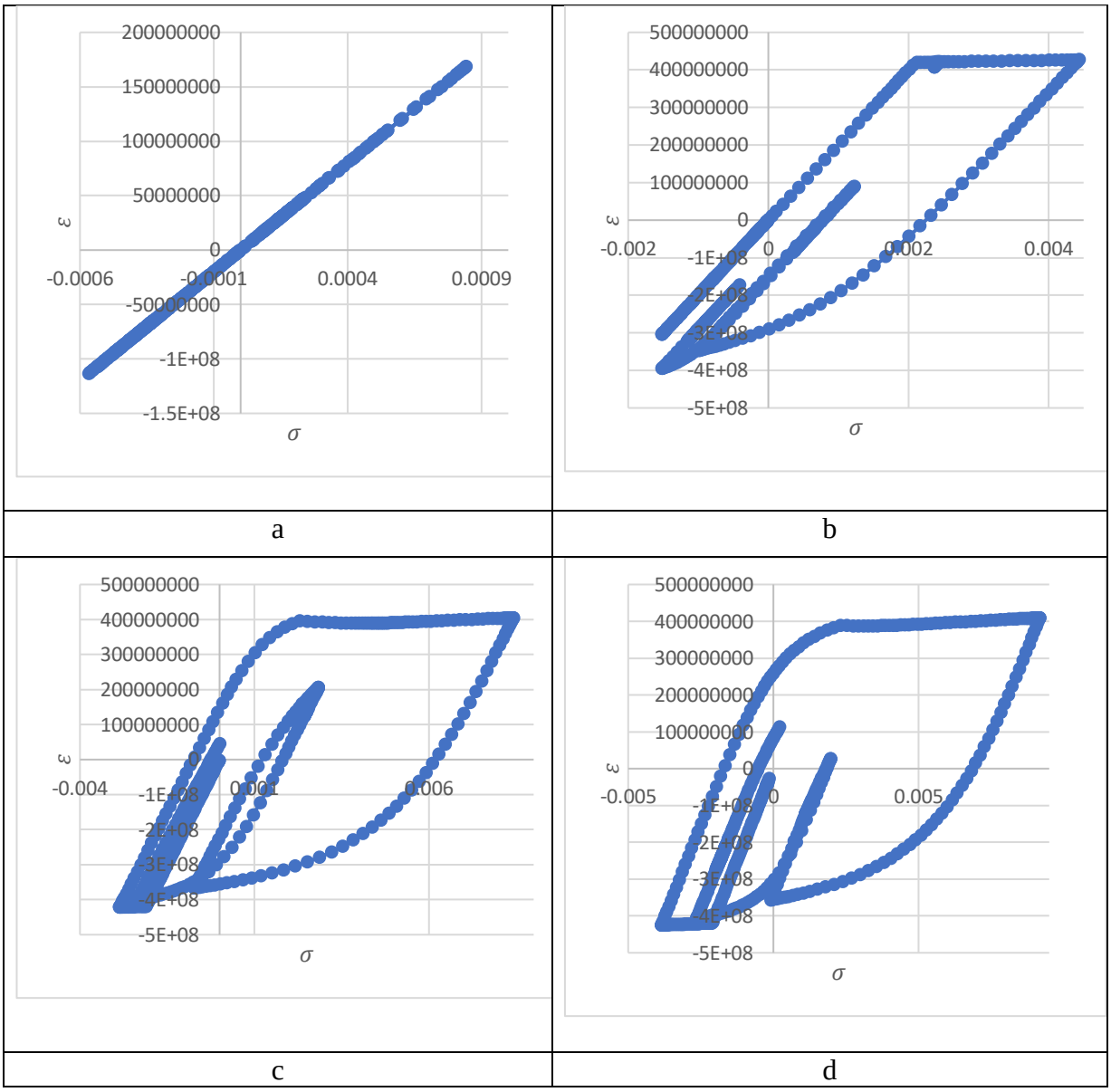

Figure 39. *Stress vs. strain plot of the bar in the right bottom corner yz--panel in the second floor in the four buildings. (a) is 4-story building stress vs. strain plot, (b) is 8-story building stress vs. strain plot, (c) is 12-story building stress vs. strain plot, (d) is 16-story building stress vs. strain plot.*

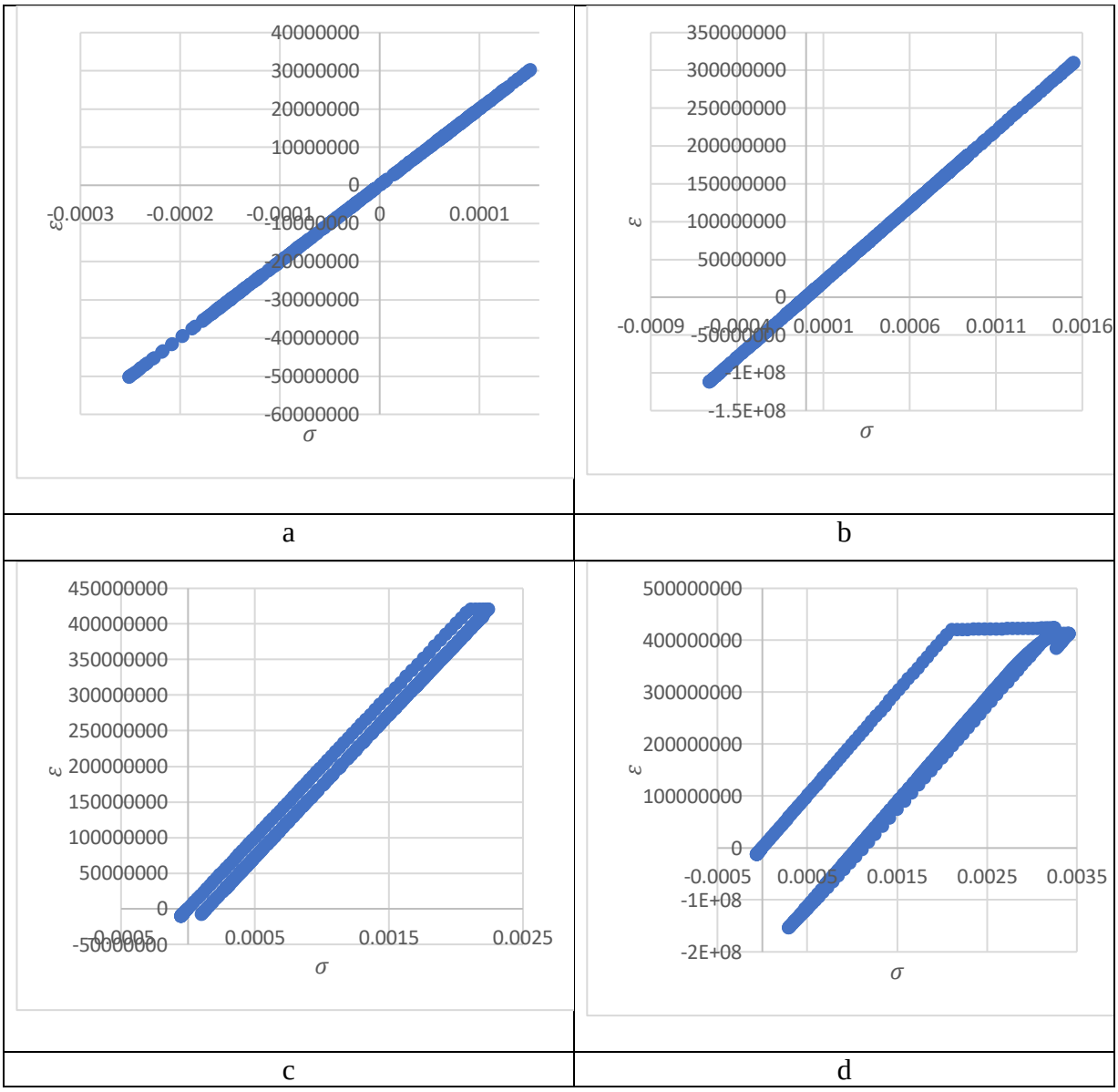

Figure 40. *Stress vs. strain plot of the bar in the left bottom corner yz--panel in the second floor in the four buildings. (a) is 4-story building stress vs. strain plot, (b) is 8-story building stress vs. strain plot, (c) is 12-story building stress vs. strain plot, (d) is 16-story building stress vs. strain plot.*